Politecnico di Milano

Faculty of Industrial Process Engineering

Department of chemistry, Materials and Chemical Engineering
“Giulio Natta”

Raman spectroscopy characterization of nanostructured Al doped ZnO films

Supervisor: Prof. Andrea Li Bassi

Co-supervisor: Valeria Russo

M.Sc. Thesis by:

Ali Maghsoumi

Student no.: 749263

Academic year: 2011 – 2012

To my family

INDEX

List of Figures

List of Tables

Abstract

Properties of ZnO as a TCO (Transparent Conductive Oxide) have improved over the last two decades by doping with different types of dopant. ZnO and aluminum doped ZnO (AZO) samples deposited by PLD in different oxygen pressure from 0.01 to 200Pa. The effects of doping and different oxygen pressure on morphology were studied by SEM and Raman spectroscopy. Then the effects of 6 months aging of AZO samples were studied by Raman spectroscopy. Also AZO samples deposited in mixed atmosphere of argon and oxygen, with different oxygen partial pressure and the effects of different oxygen partial pressure during deposition were studied by Raman spectroscopy and SEM. At last one of the AZO samples annealed in different atmosphere (Argon and vacuum) and different temperature (350^{o}C and 500^{o}C) and changes in morphology were studied by Raman spectroscopy.

Chapter1:

Introduction

Nowadays there is huge amount of attention to energy in the entire world. Searching for clear, low cost and infinite source of energy is continuing after the crises related to fossil energy. One of the sources of energy is solar energy and there is a vast amount of research on finding low cost and high-efficiency solar cells. Most of these photovoltaic technologies employ transparent conducting oxides (TCOs) as an integral part of the basic device structure.[1]

Sn-doped In2O3 thin films (In2-xSnxO3: ITO) exhibit a remarkable combination of optical and electrical transport properties. ITO has high electrical conductivity ($\sim 10^4 \Omega^{-1} cm^{-1}$) and also high optical transparency (>80%) in the visible range of the spectrum.[2] However indium is rare and also expensive material and with this amount of increasing in the usage of indium as ITO, depletion of indium resource will be problematic. In contrast, ZnO is a low-cost material and also electrical and optical properties of ZnO as a TCO have improved over the last two decades, and now have values comparable with ITO. Thus, doped ZnO can be considered as an alternative to ITO.[3] Some dopants such as Al, Si, In and Ga are often added in order to improve the electrical properties of ZnO films. Among these dopants, Al-doped ZnO (AZO) films show good electrical and optical properties.[4] Also ZnO porous films can be used as photoanode instead of TiO2 layer in Dye Sensitize Solar Cells (DSSCs) and hybrid cells.[5]

The synthesis of AZO is done by different methods. Pulse laser deposition (PLD) is a good candidate for the preparation of the AZO films because with it is possible to obtain films with different morphologies and almost tune the stoichiometry of the O vacancies and Al doping concentration that affect free carrier concentration and mobility; also it is possible to obtain better efficiency in terms of conductivity.[3, 6, 7] Film growth and chemistry may be enhanced or modified by the type and pressure of the background gas and also the temperature.[8]

This thesis is a part of a larger project. In this project the synthesis of the AZO is done by changing the type and the pressure of the background gas during deposition by PLD, and then the structural properties and also the optical and electrical properties were measured. At high pressure of background gas, nanostructured AZO were produced. Usually the AZO growth by PLD occurs with heating the substrate holder, but in this project the deposition done at room temperature and then annealing treatment was done to promote film crystallization phenomena and chemical compositional changes. Deposition was done by collaboration of a Ph.D. student in oxygen, argon and also mixtures of them; also the total pressure was changed from 0.01Pa to 200Pa. The annealing procedure was done at 350^{o}C and 500^{o}C, in Argon and Oxygen atmosphere. The structural properties were measured by Raman spectroscopy with green and blue wavelength excitation, and Scanning Electron Microscopy (SEM).

Object of this thesis is to understand the exact meaning of AZO Raman peaks and find the difference of Raman spectrum of AZO and ZnO. First the Raman spectra of ZnO were measured and used as reference for analyzing the Raman spectra of AZO. Then the effect of different oxygen pressure during deposition on structural properties of AZO was analyzed. After that the effect of aging on AZO Raman spectrum was analyzed. Then structural properties of samples that deposited in mixed atmosphere of argon and oxygen were analyzed, and finally AZO samples were annealed and effect of annealing was analyzed.

Chapter2:

Materials

2.1 ZnO

Zinc oxide (ZnO) is a wide bandgap (~3.3 eV) II-VI compound semiconductor. It is a material of wide range application. It has received much attention over the past few years for its unique properties. It has a wide range of properties that depend on doping, including a range of conductivity from metallic to insulating (including n-type and p-type conductivity), high transparency, piezoelectricity, wide-bandgap semiconductivity, room-temperature ferromagnetism, and huge magnetooptic, chemical-sensing effects. At present, the most widely publicized application for ZnO is as ITO replacement for displays and photovoltaic panels, where ZnO could lower costs of transparent conductors. But new applications for ZnO are much broader than that. In addition to its conductive nature, ZnO also can be used as a semiconductor for making inexpensive transistors for disposable electronics. ZnO is also finding applications in thin-film batteries, and ZnO ability to be engineered into interesting nanostructures hints at new applications down the road.[9, 10, 11, 12, 13]

ZnO has a stable wurtzite structure with lattice constants a = 0.325 and c = 0.521 nm.[9,10, 11, 12] Table 2.1 lists the basic physical properties of bulk ZnO. Without much effort, ZnO can be grown in many different nanoscale forms, thus allowing various novel devices to be achieved. ZnO nanostructure can be produced via different methods including chemical vapor deposition, aqueous solution growth, thermal evaporation, electrodepositing, and pulsed laser deposition, etc.

Selective element doping offers a method to adjust the electrical, optical and magnetic properties of ZnO films, which is important for applications. Many types of dopants have been introduced (e.g. Sn, As, S, Cd, FeCo, In, Cu, Mn, Al etc.). Typical dopants that have been employed to increase the conductivity of ZnO also by creation of oxygen deficiency in pure ZnO, are group III (B, Al, In, Ga) and group IV (Pb, Sn) elements of the periodic table. Table 2.2 shows some doped films, their transmittance in the visible range, the lowest resistivity values and the usual deposition method.[10]

Table 2.1: Physical properties of wurtzite ZnO[12]

Properties	**Value**
Lattice parameters at 300 K a_0 c_0 a_0/c_0 u	 0.32495 nm 0.52069 nm 1.602 (ideal hexagonal structure shows 1.633) 0.345
Density	5.606 g/cm^3
Stable phase at 300 K	Wurtzite
Melting point	2248 K
Thermal conductivity	0.6, 1-1.2
Linear expansion coefficient (/°C)	a0: 6.5×10^{-6} c0:3.0×10^{-6}
Static dielectric constant	8.656
Refractive index	2.008, 2.029
Energy Gap	3.4 eV, direct
Intrinsic carrier concentration	< 10^6 cm^{-3} (max n-type doping > 10^{20} cm-3 electrons; max p-type doping <10^{17} cm^{-3} holes
Exciton binding energy	60 meV
Electron effective mass	0.24
Electron mobility at T = 300K for low n-type conductivity	200 cm^2/V s
Hole effective mass	0.59
Hole Hall mobility at T = 300K for low p-type conductivity	5-50 cm^2/V s

Table 2.2: Different doped ZnO films as transparent conductors[10]

Dopant	**Transmittance in visible range**	**Lowest resistivity**	**Methods**
Al	~90%	~10^{-4} Ωcm	Pulsed laser deposition (PLD) Radio-frequency (RF) magnetron sputtering Solution processed
Ga	~85%	~10^{-3} Ωcm	PLD Solution processed
In	~80%	~20 Ωcm	Solution processed
N	~80%	~10^{-2} Ωcm	Plasma-assisted molecular beam epitaxy RF magnetron sputtering Solution processed

2.2 AZO

In this part the structural properties of AZO will be introduced and also the main deposition methods and the parameters that affect the deposition will be described; and one of the most important applications of AZO in solar cells and the electrical and optical properties of AZO will be reviewed.

2.2.1 Structure

Doping is an effective and facile method to modify the physical properties (e.g. optical, magnetic and electrical) of the base materials and this will extend the applications of the base materials. Al-doped ZnO (ZnO: Al) is produced by doping ZnO with Al. It has been widely used as a transparent conducting oxide (TCO) to fabricate transparent electrodes for solar cells, flat panel display devices and light-emitting diodes, because ZnO:Al exhibits low resistivity, high carrier concentration, nontoxicity, low cost, abundance in nature and high stability against hydrogen plasma which is an unavoidable processing ambient in silicon-related fields.[14, 15, 16, 17]

ZnO is naturally an n-type semiconductor because of a deviation from stoichiometry due to the presence of intrinsic defects such as O vacancies and Zn interstitials. N-type doping of ZnO is relatively easy compared to p-type doping. Group-III elements, Al, Ga, and In as substitutional elements for Zn and group-VII elements, Cl and I as substitutional elements for O can be used as n-type dopants. When ZnO is doped with group III elements, it is expected that the dopants act as singly charged donors and supply the excess carriers to conductance band, which will increase the conductivity.[18, 19, 20, 21]

Microstructure, optical and electrical properties of AZO depend on several factors such as the preparation technique, the amount of Al and the annealing temperature and atmosphere. It is possible to produce AZO thin films by different methods such as pulsed laser deposition (PLD), magnetron sputtering, sol-gel, chemical vapor deposition (CVD).[14-21]

The crystal structure of the AZO films that are deposited by PLD in low pressure or Sputtering was determined by XRD and usually shows high intense (002) diffraction peak of the wurtzite ZnO structure, which indicates the AZO films grow along <0001> direction. No diffraction peaks from the possible secondary phases, such as Zn, Al, Al2O3 and the ternary phase of ZnAl2O4, were detected, suggesting that aluminum may substitutionally replace zinc in the hexagonal lattice, interstitially exist in the ZnO lattice or segregate into the non-crystalline region in grain boundaries.[22-25] When Al ions substitute the Zn ions in ZnO, the lattice parameters decrease because the ionic radius of Al^{3+} (0.54 nm) is smaller than that of the Zn^{2+} (0.74 nm), this makes to the (002) peaks of ZnO shift to higher 2θ values with increasing of Al amount.[22, 26] For Al concentration higher than 2%, a shift is observed from (002) to (101) growth direction. This results show that when the Al concentration is less than 2%, the c-axis is perpendicular to surface of the film. When it exceeds 2%, the c-axis is tilted 58^{o} with respect to the normal surface. It is attributed to the fact that the Al atoms occupy the interstitial sites in addition to the substitutional site.[25, 26, 27] XRD patterns of AZO with different amount of Al concentration deposited by RF magnetron sputtering are shown in figure 2.1.

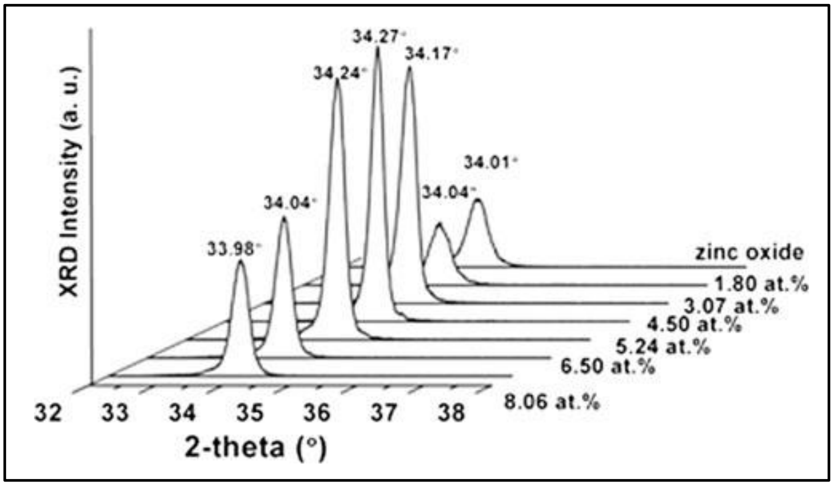

Figure 2.1: XRD pattern of AZO films with different Al concentration[22]

Surface morphologies of the Al doped ZnO thin films deposited by PLD or sputtering onto silicon (Si) substrates measured by scanning electron microscopy (SEM) show that the surface morphology of the deposited films is characterized by a smooth surface without any voids and cracks and the crystallite size of the deposited films decreases with an increase of the concentration of Al, also measuring the crystallite size by Debye-Scherer equation confirms this matter, where D is crystallite size, λ is the wavelength of the X-ray used, θ is half the angle between the incident and scattered X-ray and β is the full width at half maximum (FWHM) of the 2θ peak.[22, 24, 26]

$$D = \frac{0.94\lambda}{\beta cos\theta} \tag{1}$$

2.2.2 Deposition techniques

The synthesis and characterization of zinc oxide and doped zinc oxide via different techniques were attracted considerable attention due to their application prospects in the development of materials area. Many physical and chemical techniques have been employed in the deposition of AZO thin films. DC and RF magnetron sputtering, sol-gel, chemical vapor deposition (CVD), spray pyrolysis and pulsed laser deposition (PLD) are among them. Nowadays, pulsed laser deposition (PLD) technique has been realized to be useful in growing high quality thin films of metal oxide materials compared with other techniques.[27, 28, 29, 30, 31, 32]

The highly energetic sputtered particles present during sputtering may damage the substrate or the underlying film. Spray pyrolysis or sol–gel methods require high processing temperatures, for example (500 ^{0}C) to recrystallize the as-deposited ZnO. Such high temperatures may result in damage to low-melting point substrates or underlying films. Lower deposition temperatures are, in particular, required for thermally sensitive substrates. For example, the acceptable deposition temperature for plastic substrates required to realize lightweight plastic flat-panel displays (FPDs) or solar cells is less than 150 ^{0}C. PLD is a candidate for the preparation of transparent conductive oxide films without damaging the substrate or the underlying film.[3, 20, 33]

2.2.2.1 Magnetron sputtering (MS)

Sputter deposition is a physical vapor deposition process for depositing thin films; sputtering means ejecting material from a target and depositing it on a substrate such as a silicon wafer. The target is the source material. In the basic sputtering process, a target (or cathode) plate is bombarded by energetic ions generated in glow discharge plasma, situated in front of the target. The bombardment process causes the removal of target atoms, which may then condense on a substrate as a thin film.[34, 35] Sputtering power and substrate temperature are two main factors that affect the deposited structure. RF sputtering was developed to enable the sputtering of dielectric materials and has the double advantage that it will sputter metals as well. Main advantages of sputtering are high deposition rates, ease of sputtering any metal, alloy or compound, high-purity films, extremely high adhesion of films, excellent coverage of steps and small features, ability to coat heat-sensitive substrates, ease of automation and excellent uniformity on large-area substrates. [36]

RF magnetron sputtering is used for depositing AZO. XRD patterns of AZO films deposited under different sputtering powers and substrate temperatures show at low sputtering powers and substrate temperatures, three main diffraction peaks of ZnO; (100), (002) and (101) crystal planes, indicating no preferred crystalline orientation in the films. With increasing sputtering power to 150W or substrate temperature to 100 °C, higher energy for the regular arrangement of incident atoms promoted the growth of the AZO films in a low-energy (002) direction, then enhancing the formation of more obvious (002) preferred orientation. With higher sputtering powers, the grain size increased from 11.0 to 14.1 nm since the higher energy of incident atoms promoted grain growth. At higher substrate temperatures, the grain size even increased from 11.2 to 17.5 nm and the surface roughness decreased, because of a rapid grain growth. The AZO films deposited at low sputtering powers and substrate temperatures were made by spherical grains. As the power and temperature increased, the grains grew and became faceted with a (002) preferred orientation. [4, 27, 37]

2.2.2.2 Pulsed Laser Deposition (PLD)

The history of laser-assisted film growth started soon after the technical realization of the first laser in 1960 by Maiman. Smith and Turner utilized a ruby laser to deposit the first thin films in 1965, three years after Breech and Cross studied the laser-vaporization and excitation of atoms from solid surfaces. The technique received very little attention until the late 1980’s when high temperature ceramic superconductors were discovered and it was found that these materials could be deposited as thin films using ultraviolet light from excimer lasers. Since then, the technique of Pulsed Laser Deposition has been utilized to fabricate high quality crystalline films of complex materials with a variety of structures, from amorphous to polycrystalline or even epitaxial.[38]

Pulsed laser deposition (PLD) is a thin film deposition technique where a high power pulsed laser beam, usually ns (nanosecond) is focused inside a vacuum chamber to strike a target of the material that is to be deposited. This material is vaporized from the target (in a plasma plume) which is deposited as a thin film on a substrate (such as a silicon wafer facing the target). This process can occur in ultra-high vacuum or in the presence of a background gas, reactive gas such as oxygen which is commonly used when depositing oxides to fully oxygenate the deposited films or inert gas such as argon which is used when need to deposit in higher but inert atmosphere. Background gas is also used to produce nanoparticles at low kinetic energy. Figure 2.2 shows a scheme of PLD.[8, 38, 39]

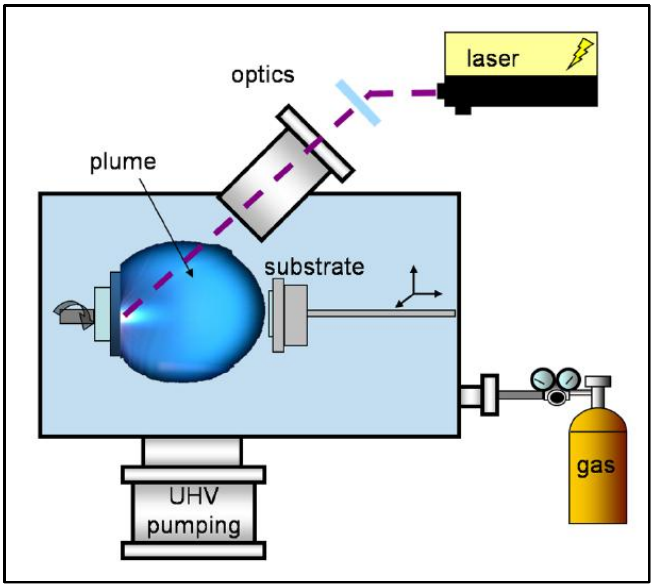

Figure 2.2: show a scheme of PLD

PLD has proven to be a successful technique for depositing films of complex oxide materials, primarily because the stoichiometry from the target is retained in the deposited films. Furthermore, PLD offers the opportunity of depositing films at low substrate temperatures, even room temperature. In addition, the film deposition can be performed in a reactive oxygen atmosphere without the need for further processing. The oxygen background atmosphere serves two purposes during PLD of metal oxide films. It may slow down and scatter the ablated target particles following a laser pulse, and it may control the oxidation state of the film surface during growth. However, the importance and interplay of each of these two mechanisms have not been clarified in detail. Also oxygen background atmosphere cause the formation of clusters or nanoparticles for nanostructured film growth [3, 39, 40]

2.2.3 PLD parameters effect on properties of ZnO and AZO films

There are 3 main parameters that affect deposition during use of PLD: deposition atmosphere, deposition pressure and deposition temperature, also it is possible to do deposition at room temperature and annealing samples after deposition. In the next part these parameters will be described.

2.2.3.1 Deposition atmosphere

The PLD technique allows preparing all kinds of oxides, nitrides, carbides, but also polymers, Buckminster fullerenes or metallic systems. In order to obtain all these different kinds of materials, one has to work in ultrahigh vacuum (UHV) or reactive gas atmosphere during deposition. This is possible with PLD, because the energy source is outside the deposition chamber. Film growth and chemistry may be enhanced or modified by carrying out PLD in an ambient background gas. Gases are often used either to thermalize the plasma species through multiple collisions, or to compensate for the loss of an elemental component of the target through incongruent ablation. Reactive PLD, on the other hand, uses gases such as H_2, CH_4, N_2, or O_2 to induce associative reactions primarily with metallic elements, to produce hydrides, carbides, nitrides, or oxides.[8, 38]

For oxide materials, proper control of the oxygen content is of paramount importance. The fact that PLD is possible in a broad range of background pressures aids especially in the formation of ferroelectric materials, for which no other method has produced better properties than those achievable by PLD. Compound targets are often employed in PLD, particularly in the production of dielectric and ceramic films and other multi elemental oxides and nitrides. This is perhaps PLD's greatest advantage over other deposition techniques, and has been most famously exploited in the thin-film growth of ceramic superconductors.[8, 39]

ZnO and AZO were deposited in different atmospheres such as vacuum, Ar, oxygen, mixture of oxygen and argon with different ratio and mixture of hydrogen and argon.[23, 40-46] Also the difference between AZO films deposited with oxygen radicals and molecular oxygen (O_2) was investigated.[3]

One of the most obvious characteristics of the PLD technique is that the surface of the film is bombarded by the high-kinetic energy ablation particles, which may cause disorder of film growth. This drawback will be serious when the film is deposited in ultrahigh vacuum environment. The bombardment by high-kinetic energy ablation particles is a key problem for epitaxial growth of high-quality films, especially in preparing devices with hetero structure interfaces. A mixture gas of hydrogen and argon in the PLD was used for overcoming the bombardment problem; argon could decrease the kinetic energy of the ablation particles, and the hydrogen would lead to the enhancement of electrical conductivity of ZnO or AZO films.[44] AZO films grown at a high oxygen regime (100 – 250 mTorr) and 750^{0}C have shown nanorod structures with a large surface roughness. On the other hand, films grown in low oxygen pressure regime and vacuum, show compact layers with small surface roughness.[41] Also researches on the AZO films deposited in mixture atmosphere of argon and oxygen show that Ar ions have decisive role for improving crystalline quality (e.g. (002) orientation) of the room temperature deposited AZO films.[46]

2.2.3.2 Deposition pressure

Background pressure in PLD can optimize the properties of the deposited films. For example oxygen pressure can change the electrical, optical and structural properties and also surface roughness of AZO thin films that were deposited by PLD. Lack of oxygen gives rise to a metal-like, shiny surface on the thin films and reduces the transmittance. On the other hand films grown in excessive oxygen atmosphere have degraded optical, electrical, and structural quality.[7, 40, 41] Kim *et al.* showed that low resistivity can be obtained only for a small range of oxygen partial pressures, between 0.53 and 0.93 Pa. The decrease in the resistivity with a decrease in the O_2 pressure, from 7.98 to 0.93 Pa, is due to a change in the number of oxygen vacancies in the films. The number of oxygen vacancies in the film increases with decreasing the oxygen partial pressure, leading to an increase in the number of free electrons.[45] Singh *et al.* showed an average transmittance about 90% in the visible range and a minimum resistivity of 1.4×10^{-4} Ωcm was obtained for AZO 2 wt% films prepared in 1 mTorr of oxygen pressure at $300^{\circ C}$. They showed that the resistivity of AZO films deposited at room temperature is more sensitive to oxygen pressure than films that were deposited at 300^{oC}.[40] Films deposited at room temperature in vacuum were amorphous and films deposited at room temperature in 0.5–3 mTorr of oxygen pressure showed the (100), (002), and (110) orientations. Films prepared in 5 mTorr of oxygen pressure showed an amorphous nature.[40] Also Lackner deposited AZO films at room temperature by PLD in O_2–Ar gas atmospheres with total pressure of 1Pa. He varied oxygen partial pressure from 0Pa to 1Pa and showed that only for medium O_2 contents in the atmosphere, (100), (101) and (002) orientated films were found, which possess a rough surface (nanocolumns). Lower oxygen contents in the deposition atmosphere result in amorphization (amorphous Zn) of the films. Higher oxygen contents lead either to amorphization on glass substrates or to the formation of high-indexed lattice planes of lattice parameters corresponding to that of the (100) Si substrates.[46]

Increasing oxygen pressure caused the 2θ position of AZO (0002) shifts to higher angle, which can be attributed to the different amounts and species of defects in AZO films.[7]

Lee *et al.* showed the surface morphology of AZO thin films varies from a uniform layer to nanorod structure by simply controlling oxygen pressure during growth. He fixed the substrate temperature to 750ºC for all depositions. In the low oxygen pressure regime (vacuum ∼50 mTorr), AZO films grow as a smooth and uniform layer and in the high oxygen pressure regime (100–250 mTorr) AZO thin films with nanorods have formed.[41]

In the case of ZnO films, the crystallite size was continuously increasing with increasing partial oxygen pressure. The crystallite size was of the order of 10 nm for films grown at low substrate temperature (200 °C) and low oxygen pressures (~10^{-4} mbar), increasing to 24 nm for films grown at high substrate temperature (500 °C) and up to 55 nm for films grown at high oxygen pressure (10^{-2} mbar).[47]

Al-doped and undoped ZnO, were highly transparent in the visible range, displaying optical transmission over 70% for pure ZnO and over 80% for Al-doped films. The dependence of VIS transmittance on the oxygen partial pressure is different for the undoped and Al-doped samples. Papadopoulou *ed al.* showed the transmittance of the AZO samples is first increasing with increasing oxygen pressure attaining the highest value for approximately 5×10^{-4} mbar and then decreasing. On the other hand, the transmittance of undoped ZnO is seen to increase with increasing oxygen partial pressure.[47]

2.2.3.3 Deposition temperature

It is possible to control the substrate temperature during deposition with PLD and it is one of the most important advantages of the PLD. Substrate temperature can effect on the growth condition and structure of the deposited material, also it is possible to optimize the electrical and optical properties of AZO thin films by controlling the substrate temperature.[40, 45]

Papadopoulou *et al.* detected, the strong (002) reflection in XRD pattern at about 34°, reflecting the wurtzite structure of the growing films with the c-axis oriented normal to the substrate. For temperatures greater than 300 °C the (004) line at 72° is also detected, indicating that the quality of the film is improving as the substrate temperature is increasing. In the case of ZnO films, the crystallite size was continuously increasing with increasing substrate temperature and with increasing partial oxygen pressure.[47]

Dong *et al.* showed the 2θ position of (0002) increased with increasing the substrate temperature from 250 °C to 500 °C. They showed this variation is related to the different strain and stress within the film. Different O content is the major origin for d_{0002} variation of AZO films deposited at different substrate temperature. Oxygen vacancies are easily formed in ZnO films. Due to a large number of O vacancies, the AZO films deposited at low substrate temperature are usually nonstoichiometric. Thus the doped Al atoms and some of the Zn atoms will locate at interstitial sites of the ZnO lattice. The large amount of interstitial atoms will lead to a great strain in AZO films and the increase in d_{0002}. When the substrate temperature increases, the mobility of O atoms on the substrate surface will increase, and O atoms can be more easily located at O sites in ZnO lattice which will lead to the increase in oxygen content in AZO films. Also with the increase in substrate temperature, the amount of interstitial atoms (i_{Zn}, i_{Al}) will decrease which will lead to the decrease in d_{0002}. Hence the 2θ position of (0002) of AZO films usually has considerable shifts toward high angle as the substrate temperature increases.[7] Also Kim *et al.* showed the FWHM values decreased, as the growth temperature increased from 250 °C to 680 °C.[45]

Singh *et al.* showed the resistivity of the AZO film decreases as the substrate temperature increases from 25 °C to 300 °C. As the substrate temperature was further increased from 300 °C to 400 °C, a slight increase in the resistivity was observed.

However, the transmittance increases continuously with the increase in the substrate temperature. This sharp change in electrical and optical properties is attributed to the structural changes.[40]

Generally, the increase in c-axis lattice parameters, calculated from the (0002) peaks for AZO films can be explained by the substitutional incorporation of Al^{3+} ions into Zn^{2+} sites and the incorporation of Al ions in the interstitial positions. This increase in lattice parameters is also related to the oxygen deficiency and strain caused by the thermal expansion coefficient mismatch between the film and substrate.[7, 40, 45]

2.2.3.3.1 Annealing procedure

Also it is possible to study the effect of temperature of a post-deposition annealing instead of substrate temperature during deposition. Post annealing is useful in the case it is impossible to change the substrate temperature, but also it is usual in PLD. The electrical resistivity of ZnO and AZO thin films can be modified by post-deposition annealing. Temperature and atmosphere of annealing are two parameters that effect on properties of ZnO and AZO thin films, since the properties of ZnO and AZO thin films depend on the non-stoichiometry of films resulting from the presence of oxygen vacancies and interstitial ions. Post-deposition annealing were done in vacuum, oxygen, nitrogen, hydrogen and in some cases mixture of them.[48-52]

Lee *et al.* showed that, with increasing annealing temperatures, the full-width at half-maximum (FWHM) of XRD spectrum became smaller, which is evidence of the improvement of the crystal quality and shows the increase in grain size of AZO thin films. Fang *et al.* showed the lattice constant “c” of the film decreased (the (002) peak of the film shifted towards a high angle) after the annealing process; because the residual stress of the film can be reduced by annealing process that resulted in a peak shift of XRD patterns toward high angle. Lenon *et al.* said the relaxation in strain may be associated with diffusion of interstitial Al atoms into Zn lattice sites.[48, 49, 50]

Annealing in oxygen was proved to be slightly more effective than vacuum annealing in improving the crystal quality. The grain size of the AZO thin film annealed in oxygen ambient is larger than for that annealed in a vacuum.[48]

AZO films generally exhibit an n-type conduction behavior due to electrons supplied from donor sites associated with oxygen vacancies, high-valence metal ions or zinc interstitial. Different annealing condition resulted in an apparent influence on the electrical properties of the AZO films. The resistivity of the AZO films continuously increased with increasing annealing temperature from 500 °C to 700 °C; the resistivity of the thin film annealed in oxygen ambient was higher than for that annealed in vacuum which was related to the decrease of carrier concentration resulting from the increase of oxygen content and the change of oxygen states. The carrier concentration of the AZO films decreased with increasing annealing temperature, but the value for the AZO thin film annealed in oxygen ambient was much smaller than for that annealed in a vacuum. Oxygen atoms incorporated during the oxygen annealing process reduced the concentration of carrier-like electrons in the AZO films.[48, 49] Oh *et al.* showed the resistivity of the hydrogen-annealed film decreased which is accompanied by the increase in the carrier concentration. In general, resistivity of the films is mainly affected by carrier concentration and mobility. Since the increase of the carrier mobility in the case of hydrogen annealing was small compared to the increase of carrier concentration, the improved electrical property is mainly due to the increase in carrier concentration. Such increase in carrier concentration is attributed to desorption of negatively charged oxygen species from the grain boundaries which act as trapping sites and form the potential barriers. The negatively charged species form depletion regions near the grain boundary surfaces decreasing free-carrier concentration and Hall mobility. If these depletion regions in the AZO films were removed by the passivation of the grain boundary surfaces during the post-deposition annealing in hydrogen atmosphere, carrier concentration and Hall mobility would increase. Since the Al contents in the films did not change during the annealing process, as mentioned above, it is believed that passivation of grain boundary surfaces by hydrogen is the main reason for the improved electrical properties.[51]

With increasing annealing temperature, the band gap of the thin film decreases. The band gap of the film annealed in oxygen was lower than that annealed in vacuum.[48, 49]

Lennon *et al.* showed the average visible transmittance increased after annealing in N_2. The poor optical properties exhibited by as-deposited films were a result of metallic Al interstitials which had not been incorporated into the ZnO lattice. Upon annealing, metallic Al atoms diffuse through the ZnO matrix and are incorporated as substitutional impurities on Zn lattice sites. It is also conceivable that a reduction in optical scattering associated with larger grains can contribute to the improvement in transmittance; however, in light of the relatively small increase in grain size, this effect is considered to be negligible.[50, 52]

2.2.4 Application

ZnO have high transparency in the visible and near-ultraviolet spectral regions, wide conductivity range and conductivity changes under photoreduction/oxidation condition. Accordingly this binary compound has wide applications in chemical sensors, heterojunction solar cells, electrophotography, surface acoustic wave devices, conductive transparent conductors and many others. However, pure ZnO thin films lack stability in terms of thermal aging in air or corrosive environments. Therefore polycrystalline ZnO films have been doped with group II and group III metal ions such as indium (In), aluminum (Al), gallium (Ga), copper (Cu), cadmium (Cd) etc. to enhance structural, optical and electrical properties. Doping is particularly done to get high transparency, stability and high conductivity. Aluminium doping is particularly suitable for this purpose. AZO thin films have high transmittance in the visible region, and a low resistivity, and the optical band gap can be controlled by using Al doping amount. Accordingly they have got potential applications as TCO in solar cells, large flat-panel displays, low-emissivity and electrochromic windows etc. [3, 21, 53]

2.2.4.1 Transparent conducting oxide (TCO)

Nearly all of photovoltaic (PV) technologies employ transparent conducting oxides (TCOs) as an integral part of the basic device structure. These solar cell architectures are based on the use of new lower - cost semiconductors, thin films of conventional semiconductors, and organic–inorganic hybrids, and many are rapidly attaining commercial viability. Each PV technology has different requirements for the TCO layer, leading to a reexamination of these materials. Coupled to this is an effort to make conventional cells more efficient by improving the junction characteristics. There is an increasing desire to employ TCO layers as diffusion barriers, to control the contact work function, to provide an interface with organic and other materials and to have the TCO also act as a light trap. Low process temperatures and increased process flexibility are critical for many devices. This need for improved performance in a wide range of areas coupled with the ever-rising price of In is driving a renaissance in the investigation of novel TCOs for PV applications. PV devices require at least one electrode that can provide both optical access and a low-resistance electrical connection. Materials that combine optical transparency over much of the solar spectrum with reasonable electrical conductivity generally fall into three classes: very thin pure metals, highly doped conjugated organic polymers, and degenerately doped wide-bandgap oxide or nitride semiconductors. For PV applications, the choice of TCO is driven by additional considerations, including work function, band alignment, materials compatibility, processing, and cost.[1]

Transparent conducting oxides (TCOs) comprise a class of materials that can be thought of as conjugate property materials in which one property, in this case conductivity, is strongly coupled to a second property, namely, the lossy part of the refractive index or the extinction coefficient. In this regard, materials, like metals, that are highly conductive, will not normally transmit visible light, while highly transparent media like oxide glasses behave as insulators. The challenge for achieving materials that are both conducting and optically transmissive is to understand the fundamental materials structure/property relationships that drive these properties so that they may be decoupled such that the material both retains transparency while becoming electrically conductive.[31]

The first TCO was reported in 1907 by Baedeker who used a primitive vapor deposition system to deposit thin film CdO that was both optically transparent and electrically conducting.[1, 31]

The optical and electrical performance of TCOs is intimately tied to the fundamental band structure of the material and, therefore, periodic distribution of potential in the crystal. This would, at first glance, suggest that amorphous materials, where the long-range order of the crystalline structure has been disrupted, would yield materials with dramatically different optical and electrical properties. In the case of indium oxide, this proves to be not the case, and both the crystalline and amorphous states of indium oxide, as will be discussed, yield usable TCO materials. Oxides with a fundamental bandgap of 3eV or more are insulators at room temperature in the undoped state. To become conducting, the oxide must be doped to degeneracy by increasing the free carrier density enough to move the Fermi level into the conduction band. Degenerate doping requires a source of electron donors in the form of point defects (often oxygen vacancies) or impurities with ionization energy close to the conduction band; this severely limits the selection of TCO materials.[1]

In some oxides such as indium oxide, zinc oxide, tin oxide, and cadmium oxide, native stoichiometric point defects like oxygen vacancies are readily ionized and thereby donate electrons to the conduction band. Further doping is usually required (for example, Al in ZnO, Sn in In2O3, and Sb in SnO2), and these dopants must find substitutional sites in the lattice. This high level of ionized impurities in the form of charged native point defects or impurity atoms typically leads to a decrease in carrier mobility (μ) and represents a tradeoff when optimizing the resistivity of the material.[1, 31]

One of the important transparent conductive oxide used in photovoltaic (PV) window and display technology applications is doped ZnO, which has been reported to have a thin film resistivity as low as 2.4×10^{-4} Ωcm. Although the resistivity of ZnO thin films is not yet as good as the ITO standard, it does offer the significant benefits of low cost relative to In-based systems and high chemical and thermal stability. In the undoped state, zinc oxide is highly resistive because, unlike In-based systems, ZnO native point defects are not efficient donors. However, reasonable impurity doping efficiencies can be achieved through substitutional doping with Al, In, or Ga. Most work to date has focused on Al-doped ZnO, and this dopant requires a high degree of control over the oxygen in the deposition because of the high reactivity of Al with oxygen.[1, 31]

The current understanding of conductivity in transparent materials is based upon a classical description of charge transport in metals coupled to the optical properties of the material through the density of charge carriers and their effective mass. A summary of the key concepts provided below defines the relevant parameters used to describe the performance of these materials. These include the conductivity (σ), sheet resistance (R_s), free carrier mobility (μ), free carrier density (N), and the imaginary or lossy part of the refractive index termed the extinction coefficient (κ) that is proportional to the absorption coefficient (α) through the wavelength (λ).

$$I = I_0 \exp(-\alpha d)\,, with \frac{4\pi\kappa}{\lambda} \qquad (2)$$

Here, I_0 is the incident light intensity on a material of thickness d, and I is defined as the transmitted intensity through the material. Proper use of this equation for thin films requires that optical scattering and reflection losses at the interfaces be considered. A quantitative measure of performance of a TCO can be written in terms of the ratio of the electrical conductivity to the optical absorption coefficient or,

$$\frac{\sigma}{\alpha} = 1[R_s \ln(T + R)]^{-1} \qquad (3)$$

Where, T and R represent the total transmittance and reflectance of the material, and R_s is the sheet resistance (= resistivity/film thickness). This figure-of-merit is used to assess the relative performance of different TCO materials and is wavelength dependent. It should be noted here that the factors appearing in Eq. (3) are highly dependent upon processing conditions and hence, the resident microstructure and defect chemistry of the material. Thus, a highly optically scattering material, due to the presence of a polycrystalline grain structure, will have both diminished transmission, and higher resistivity due to a decrease in charge mobility arising from scattering of charge carriers at grain boundaries. The figure-of-merit provides a good qualitative estimate of TCO performance for materials having similar microstructure.[2, 31]

2.2.4.2 Photovoltaic application

Most photovoltaic cells produced are currently deployed for large scale power generation either in centralized power stations or in the form of building integrated photovoltaics (BIPV). BIPV is receiving much attention, as using photovoltaic cells in this way minimizes land use and offsets the high cost of manufacture by the cells (or panels of cells) acting as building materials. Although crystalline Si solar cells dominant cell type used through most of the latter half of the last century and now, other cell types have been developed that compete either in terms of reduced cost of production (solar cells based on the use of multicrystalline Si or Si ribbon, and the thin-film cells based on the use of amorphous Si, CdTe, or CIGS) or in terms of improved efficiencies (solar cells based on the use of the III-V compounds). All of these semiconductors have energy bandgaps within the range 1.1-1.7 eV, they are near to the optimum energy bandgap (1.5 eV) for photovoltaic solar energy conversion by a single junction solar cell.[54]

We can classify PV solar cells in five groups:[1, 54, 55]

A. Si-Based Cells: Crystalline, Multicrystalline, Amorphous Si solar cells, and heterojunction with intrinsic thin layer (HIT) cell.

B. Thin-film solar cells based on compound semiconductors: Cadmium Telluride (CdTe) thin-film solar cells and solar cells based on chalcopyrite compounds.

C. III-V solar cells: single junction III-V solar cells, and III-V multijunction devices.

D. Dye-Sensitized Solar Cells (DSSC).

E. Organic/Polymeric solar cells.

A) A cross-sectional view of the Si solar cell structure that has been used in production up to the present is given in Figure 2.3. For crystalline Si devices, a boule of B-doped p-type Si is grown using the Czochralski method and wafers are sawn from the boule. Crystalline (and multicrystalline) Si has an indirect energy bandgap resulting in a low optical absorption coefficient, with the consequence that the wafers need to be greater than 200 μm thick to absorb most of the incident light. The wafer surfaces are ‘textured’ by dipping into a solution of NaOH and isopropyl alcohol to minimize reflection losses and to refract light entering the Si to high angles of refraction and enhance the optical path length in the Si. A p-n junction is formed by diffusing phosphorus into the wafer as an impurity dopant. Screen-printed Ag contact fingers are used on the n-type surface to make electrical contact while also allowing light to be transmitted to the junction region. Al paste is used to make contact at the back p-type surface. This is annealed to introduce a p^+ doped region at the back of the cell to lower the contact resistance and supply a back surface field that reflects minority carriers back toward the junction. An antireflection (A/R) coating (usually TiO2 or silicon nitride) is deposited over the top surface to complete the device.[54]

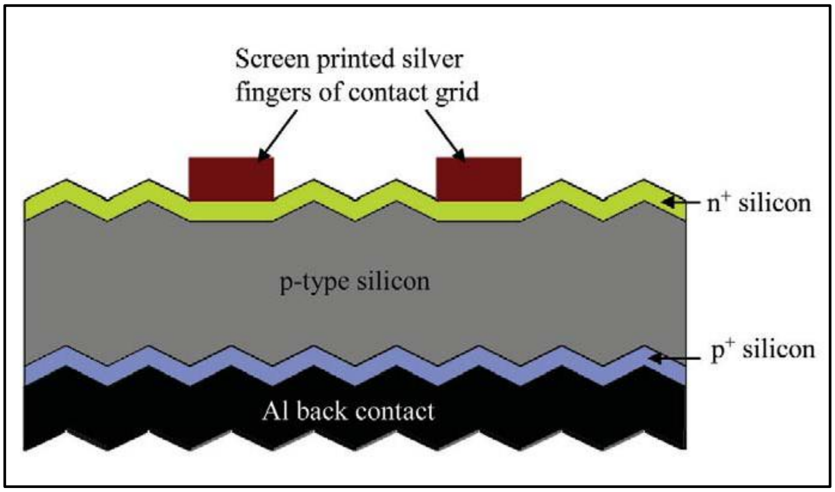

Figure 2.3: Cross-sectional view of solar cell produced with screen-printed contacts.[54]

The HIT cell, as shown schematically in Figure 2.4, has achieved record efficiencies (19.2% in commercial PV modules) for simple cell geometry. The structure consists of a crystalline silicon layer with an amorphous top junction that is contacted by a TCO layer (typically ITO) and a metallic collection grid.[1]

Amorphous Si solar cells use TCOs as a top contact layer, as shown in Figure 2.4, and in cells fabricated on glass substrates, it is common to employ a second TCO layer on the glass side. This buried TCO layer is typically fluorine- doped SnO2 or crystalline ITO. The top layer in the a-Si *n-i-p* cell shown in Figure 2.4 usually is Ga-doped ZnO, which is a material that can be deposited at low temperature as a polycrystalline film with strong texture-dependent surface morphology. Surface morphology control is increasingly important to improve light trapping as the Si part of these cells becomes thinner. The use of Ga-doped ZnO as a top-side contact also has the added benefit of reduced cost because it uses naturally abundant Zn rather than costly In. Also there are some researches that were used Al-doped ZnO instead of Ga-doped ZnO and they gained better efficiency.[1, 56]

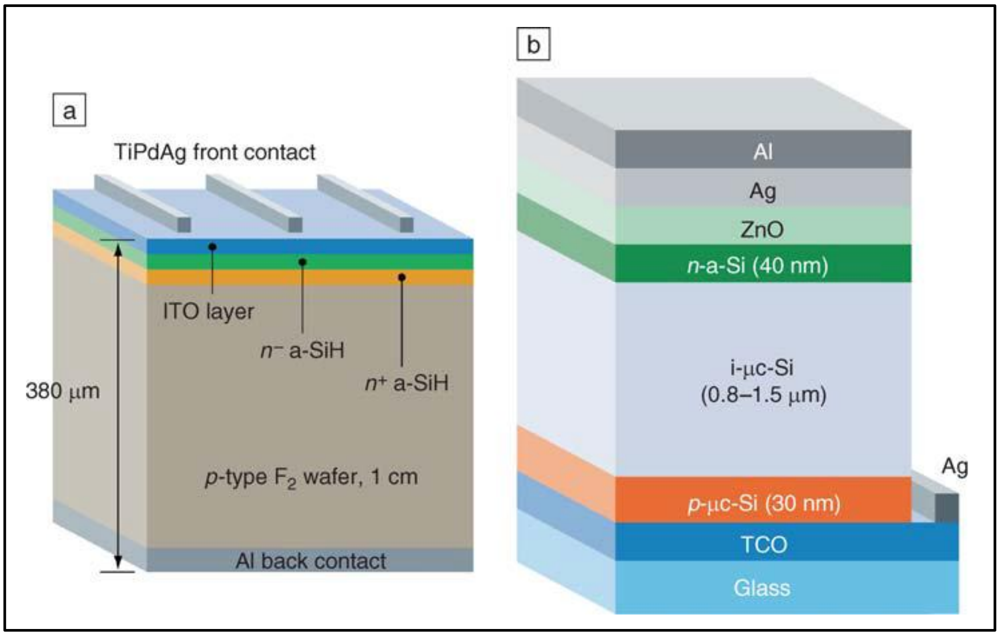

Figure 2.4: Typical configuration for (a) HIT cell and (b) an amorphous Si n–i–p cell. In (b), i stands for intrinsic, μc is microcrystalline, and a is amorphous.[1]

B) Copper indium gallium selenide (CIGS) and cadmium telluride (CdTe) thin – film solar cells have demonstrated efficiencies near 20% in the laboratory. With a direct optical energy bandgap of 1.5 eV and high optical absorption coefficient for photons with energies greater than 1.5 eV, only a few microns of CdTe are needed to absorb most of the incident light. Because only thin layers are needed, material costs are minimized, and because a short minority diffusion length (a few microns) is adequate, expensive materials processing can be avoided. In CdTe cells, a front contact is provided by depositing a TCO onto the glass substrate. This is followed by the deposition of a CdS window layer, the CdTe absorber layer, and finally the back contact. The requirements for the top TCO contact in CIGS cells are both demanding and unique to this technology. The defect chemistry of CIGS is complex, and the active layers in these cells are highly temperature sensitive and susceptible to defect and impurity diffusion. To maintain stoichiometry at the surface and to prevent point defect creation caused by selective evaporative loss at the surface, a stabilizing thin layer of CdS is used to cap the CIGS and to form the initial contact junction with the TCO layer deposited above it. The CdS layer is normally deposited at room temperature in a wet chemical bath process. The TCO top layer must likewise be applied at low temperature; even then, when doped ZnO is deposited directly on the CdS cap, junction leakage currents are observed. Experience shows that these problems can be avoided by depositing a thin layer of undoped TCO, then a thicker layer of doped TCO, onto the CdS. Typically the TCO used in these applications has been AZO.[1, 54]

C) The III-V compounds, such as GaAs, InP, and GaSb, have direct energy bandgaps, high optical absorption coefficients, and good values of minority carrier lifetimes and mobilities (in highly pure, single crystalline material). This makes them excellent materials for high efficiency solar cells. The III-V materials are used for making single-junction solar cells are GaAs and InP, as both have near optimum energy bandgaps of 1.4 eV.

In a single-junction Si solar cell, 56% of the available energy is lost because photons with energies less than the bandgap are not absorbed, and photons with energies greater than the bandgap ‘thermalize’, such that the excess energy over the bandgap is lost as heat. A range of studies have shown that using multijunction solar cells, such losses can be minimized leading to much higher efficiency devices.[54]

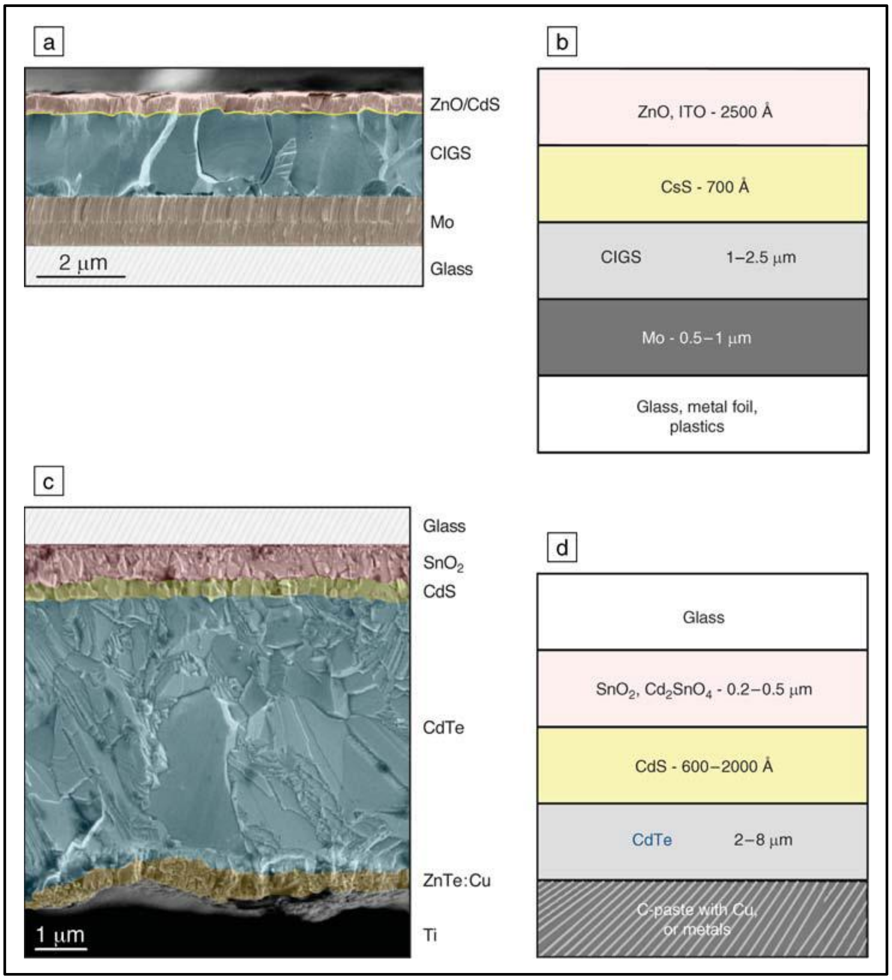

Figure 2.5: (a) Copper indium gallium selenide (CIGS) and (c) CdTe seen in cross section using SEM. (b), (d) Schematic illustrations of the structures in (a) and (c), respectively.[1]

D) DSSCs have been reported to challenge conventional solid state photovoltaic devices based on the p-n junction diode. A typical DSSC consists of a TCO substrate, a dye-sensitized semiconductor oxide layer, a liquid redox electrolyte, and a Pt-coated counter electrode. The DSSC, illustrated in figure 2.6, is a new approach to PV that uses nanoparticles of dye sensitized TiO_2 to collect electrons from electron-hole pairs created by photon interaction at a dye/TiO_2 interface. The holes are transported via aqueous ionic mediators for collection at TCO counter electrodes.

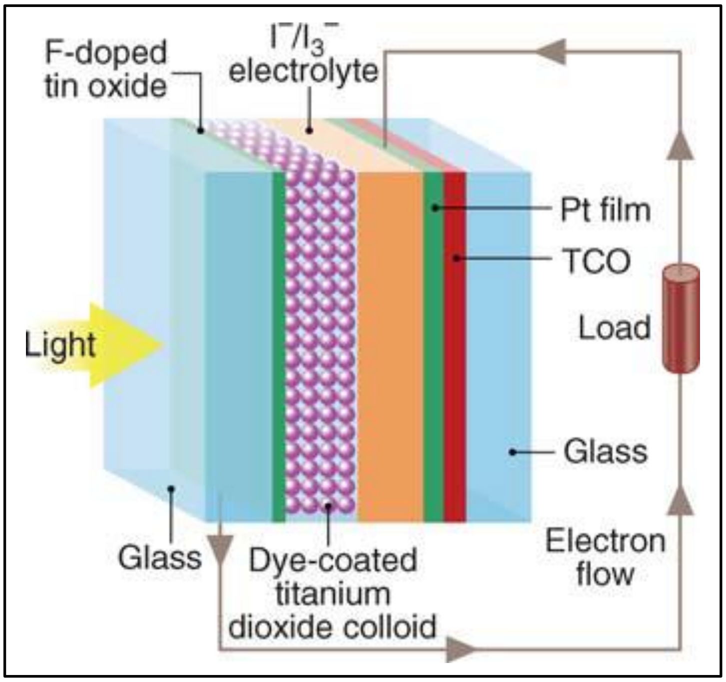

Figure 2.6: Schematic view of the Grätzel dye Sensitized solar cell, showing the use of a TCO from contact and dye-sensitized nanocrystalline TiO_2 particles.[1]

The DSSC, which is the most efficient and stable excitonic cell, has been widely investigated due to its low fabrication cost and relatively high efficiency, compared to conventional silicon solar cells. DSSC anodes are typically constructed of TiO_2 nanoparticle films. ZnO, with a similar bandgap and comparable electron injection process to that of TiO_2, has been proven to be one of the most promising alternative photoelectrode materials for application in DSSCs. Compared to ZnO (TiO_2) nanoparticle films, single crystals of these materials exhibit significantly faster electron transport and greater electron mobility. The faster electron transport is a result of the high electron diffusion coefficients, which will provide significant advantages to device performance. The greater electron mobilityis due to the directional and uninterrupted conduction channel, which can improve the efficiency of charge collection and enable the production of optically thick cells which absorb more incident light. In spite of the improved charge transport and the larger electron mobility, one-dimensional (1D) ZnO nanowires show a smaller total surface area for nanowire arrays, as compared with the best TiO_2 nanoparticle devices, which adsorb less dye per unit thickness of the cell and thus absorb less light and collect less charge. As a result, the energy conversion efficiency (μ) of ZnO nanowire-based DSSC is typically lower. But recently, AZO nanorod arrays as photoelectrode has been applied to fabricate DSSC, a large increase of the μ in AZO nanorod-based DSSCs (1.34%) as compared to undoped (0.05%) has been obtained.[1, 57, 58]

E) Conjugated polymers are excellent candidates for use in low-cost electronics and PV. Polymer-based solar cells have reached power conversion efficiencies of 5% in recent reports. In addition to the inherent economics of high-throughput manufacturing, light weight and flexibility are qualities claimed to offer a reduction in the price of PV panels by reducing installation costs. Flexible PV also opens up niche markets like portable power generation and aesthetic PV in building design. The needs of the TCO in an Organic Photovoltaic (OPV) device include work-function matching, stability on a deformable surface, the ability to protect the OPV layer from the atmosphere, and low resistivity. These requirements make the organic transparent conductors unusable for this application. Inorganic TCOs, however, are suitable and also offer the possibility of being nanostructured into filaments (e.g., ZnO nanowires) to maximize the organic/inorganic interface and to minimize the impact of the short diffusion lengths on exciton dissociation and charge carrier collection. The ideal TCO for OPVs must also have a high work function to optimize the open-circuit potential and to facilitate charge injection and also be readily wetted by the organic layer. Finally, the ideal TCO would have high mobility and high carrier density when processed using a nonvacuum, low-temperature-based deposition approach. No such TCO currently exists, but a conceptual diagram for a nanostructured TCO/polymer cell is shown in figure 2.7. Attempts to realize this design with a non-optimized structure (in terms of nanofiber spacing and properties) using ZnO nanorods and an organic (P3HT/PCBM) fullerene blend have achieved nearly 3% PV efficiency. As indicated, there is a tremendous amount of optimization needed for the TCO in this application, and it is likely that existing choices will not be adequate.[1, 55]

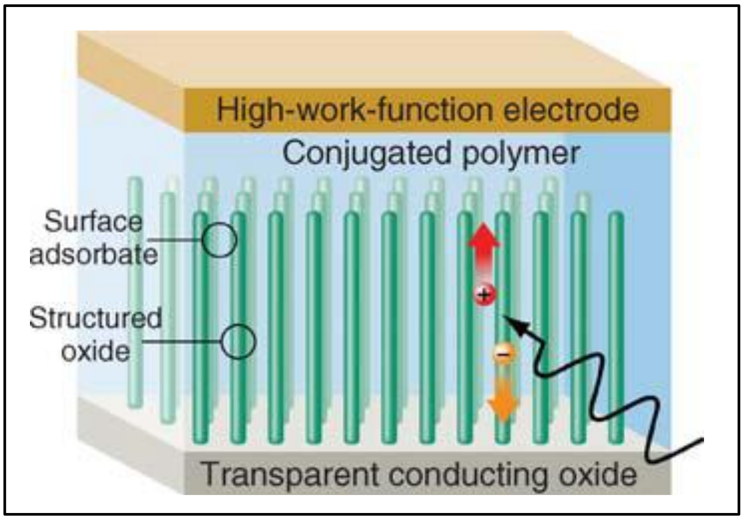

Figure 2.7: Schematic view of an organic photovoltaic cell using a nanostructured transparent conducting oxide (TCO) grown on a planar TCO layer and intercalated with a conjugated polymer.[1]

2.2.5 Electrical and optical properties

ZnO is semiconductor materials with a direct band gap of 3.3 eV and highly attractive in the development of materials area, due to their interesting physical properties as high transparency in the visible and near-ultraviolet (UV–VIS) spectral regions. In addition, doping of the IIIA ions such as Al into the lattice reduces its resistivity without any deterioration of its transmittance. Al acts as a cationic dopant in the ZnO lattice and substituted the Zn site. In ZnO, since zinc has a valence of 2, the aluminum doping in the lattice provides electrons to the conduction band and drastically increase electrical conductivity and carrier concentration. The resistivity of ZnO film dramatically decreases with Al^{3+} doping due to Al^{3+} substitution of Zn^{2+}, oxygen vacancies and Zn interstitial atoms. The resistivity (ρ) is inversely proportional to the product of the Hall mobility (μ) and the carrier concentration (n), with relation:

$$\rho = \frac{1}{e\mu n} \tag{4}$$

where e is electron charge. The minimum resistivity is achieved when both Hall mobility and carrier concentration are at a high level.[7, 22]

The conductivity and transparency of AZO thin films depends upon several factors, such as the preparation technique, the in situ preparation parameters, the amount of Al, the annealing temperature and atmosphere, and even the measurement conditions. The minimum resistivity of about 1×10^{-4} Ωcm can be attained when AZO films were grown at 250 - 350 °C and proper oxygen ambience, and average transparency can achieve more than 80% in the visible and near-infrared (NIR) regions.[7, 21, 22]

Chapter3:

Raman spectroscopy

3.1. Raman Spectroscopy

Inelastic scattering of light was predicted by Adolf Smekal in 1923, but observed in practice in 1928. Sir C. V. Raman observed the effect by means of sunlight, and then the Raman effect was named. Raman won the Nobel Prize in Physics in 1930 for this discovery accomplished using sunlight, a narrow band photographic filter to create monochromatic light, and a “crossed filter” to block this monochromatic light.[59]

Raman spectroscopy is one of the characterization technique that is used in many different materials. Raman scattering used to analyze the vibrational dynamics of the molecules or lattice cells constituting the material and it provides a sort of fingerprint of the material analyzed. It relies on inelastic scattering, or Raman scattering, of monochromatic light, usually from a laser in the visible, near infrared, or near ultraviolet range. Typically, a sample is illuminated with a laser beam. The laser light with frequency ω_L interacts with molecular vibrations, phonons or other excitations in the system, resulting in the energy of the laser photons being shifted up or down. The shift in energy gives information about the vibrational modes in the system. Light from the illuminated spot is collected with a lens and sent through a monochromator, it consists of a very strong line at the frequency ω_L, an also a series of much weaker lines with frequencies $\omega_L \pm \omega_j(q)$, where $\omega_j(q)$ are optical phonon frequencies. Wavelengths close to the laser line (ω_L) due to elastic Rayleigh scattering are filtered out while the rest of the collected light is dispersed onto a detector. The series of weak lines at $\omega_L \pm \omega_j(q)$ originates from inelastic scattering of photons by photons by phonons and constitutes the Raman spectrum. The Raman bands at frequencies $\omega_L - \omega_j(q)$ are known as Stokes lines, and bands at frequencies $\omega_L + \omega_j(q)$ are called anti-Stokes lines. The intensities of the anti-Stokes lines are usually well weaker than those of the Stokes lines. In first order of Raman scattering only optical phonons with $q \approx 0$ are involved, as a consequence of momentum conservation.[60]

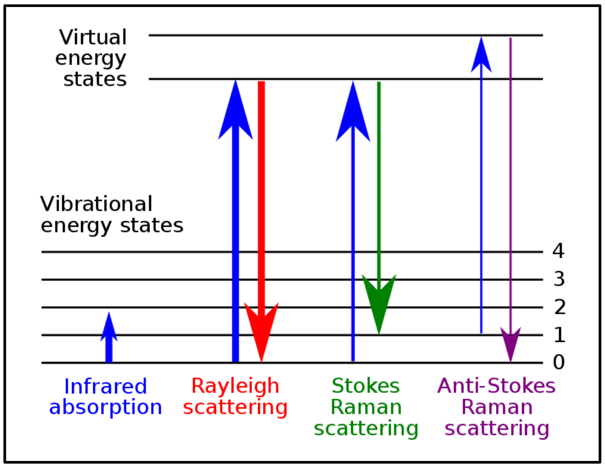

Figure 3.1: Energy level diagram showing the states involved in Raman signal. The line thickness is roughly proportional to the signal strength from the different transitions.

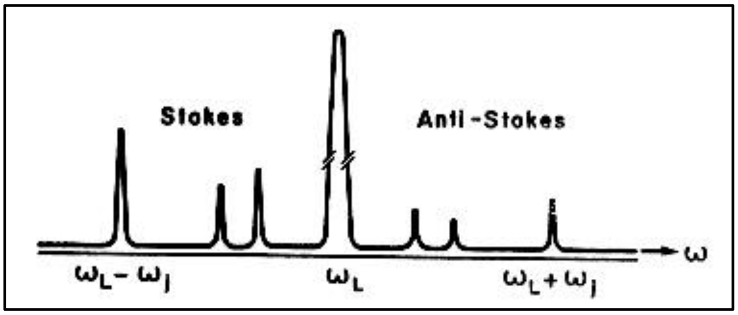

Figure 3.2: Schematic of Stokes and anti-Stokes Raman spectrum. The strong line at ωL is due to Rayleigh scattering.[60]

In common usage, Raman shifts are typically in wavenumbers with units of inverse length. The following equation used to convert spectral wavelength to wavenumbers of shifts in Raman spectrum:

$$\Delta\omega = \left(\frac{1}{\lambda_0} - \frac{1}{\lambda_1}\right) \quad (1)$$

where $\Delta\omega$ is the Raman shift expressed in wavenumber, λ_0 is the excitation wavelength, and λ_1 is the Raman spectrum wavelength. Usually, the units selected for expressing wavenumbers in Raman spectra is inverse centimeters (cm^{-1}). Since wavelength is often expressed in units of nanometers (nm), equation (1) can scale for this units conversion explicitly and expressed in form equation (2).

$$\Delta\omega\ (cm^{-1}) = \left(\frac{1}{\lambda_0(nm)} - \frac{1}{\lambda_1(nm)}\right) \times\ 10^7 \qquad (2)$$

3.2 Raman of ZnO

In the wurtzite ZnO case with C_{6v} symmetry, there are 4 atoms per unit cell and 12 phonon modes, three modes for acoustic phonon and nine modes for optical phonon, one longitudinal-acoustic (LA), two transverse-acoustic (TA), three longitudinal-optical (LO), and six transverse-optical (TO) branches. In the zinc-blende polytypes with 2 atoms per unit cell, six modes are present, three acoustical (one LO and two TO) and three optical (one LO and two TO) branches. The normal lattice vibration on the basis of group theory is $\Gamma_{opt} = A_1(z) + 2B_1 + E_1(x, y) + 2E_2$. The A_1, E_1, and the two nonpolar E_2 branches are Raman active, and the B_1 branches are inactive (silent modes). The A_1 and E_1 modes are each split into LO and TO components with different frequencies due to the macroscopic electric fields associated with the LO phonons. The TO-LO splitting is larger than the A_1-E_1 splitting due to the electrostatic forces dominate the anisotropy in the short-range forces. For the lattice vibrations with A_1 symmetry, the atoms move parallel to the c axis, and for the lattice vibrations with E_1 symmetry, the atoms move perpendicular to the c axis. The low-frequency E_2 mode is associated with the vibration of the heavy Zn sublattice, while the high-frequency E_2 mode involves only the oxygen atoms. In the case of highly oriented ZnO films, if the incident light is exactly normal to the surface, only A_1-LO and E_2 modes are observed, and the other modes are forbidden according to the Raman selection rules. Right-angle Raman scattering in ZnO for various polarization and propagation direction sufficient to define the vibration at room temperature with 4880 Å excitation were shown in figure 3.3. In the notation that is used in figure 3.3, each spectrum is described by four symbols. The symbols inside the parenthesis are, left to right, the polarization of the incident and of the scattered light, and the ones to the left and right of the parenthesis are the propagation directions of the incident and of the scattered light, respectively.[19, 20, 61]

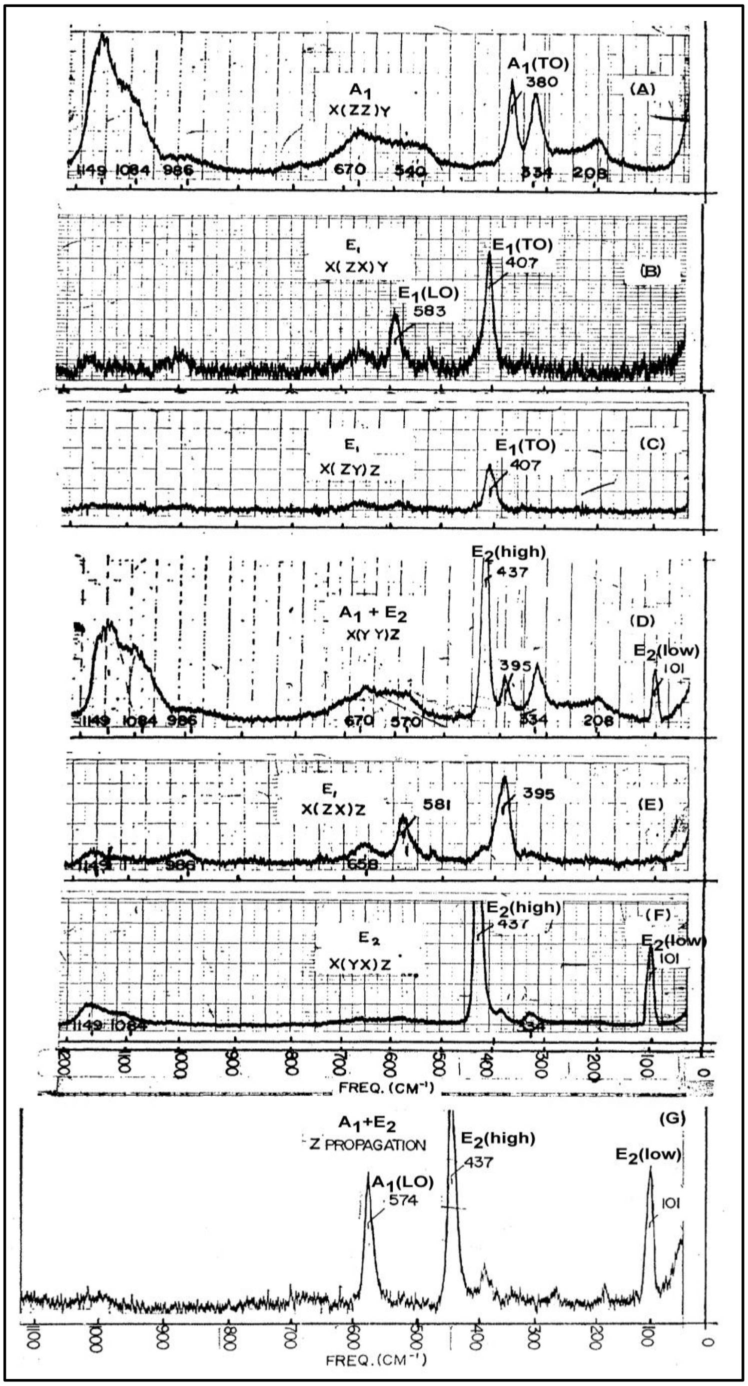

Figure 3.3: Right-angle Raman scattering in ZnO for various polarization and propagation direction at room temperature with 4880 Å excitation.[61]

In figure 3.3 (A), in the case of polarization along z direction, since the phonons propagates in the xy plane, it is pure transverse and it is the A_1-TO at 380cm^{-1}. In the case of scattered light with x polarization (part B of the figure), we can see the E_1 character; phonons vibrations decompose into parallel and perpendicular to the phonon-propagation direction, E_1-TO (407cm^{-1}) and E_1-LO (583cm^{-1}). Similarly, in part C of the figure, incident and scattered light in the xz plane, we can see the E_1 transverse phonon at 407cm^{-1}. In figure 3.3 (D and E), the phonons have “quasi transverse” and “quasi longitudinal” components and mixed character for which the A_1 character is observed in (D) and E_1 in (E). The transverse-phonon frequency for $\theta = 45^0$ is given by:

$$\nu_t^2 = \frac{1}{2}\left[\left(\nu_t^{\parallel}\right)^2 + (\nu_t^{\perp})^2\right] \qquad (3)$$

where $\nu_t^{\parallel}$ is the A_1 transverse phonon and $\nu_t^{\perp}$ is E_1 transverse phonon, and so we have peak at 395cm^{-1} for A_1-TO (380cm^{-1}) and E_1-TO (407cm^{-1}) in figure (D). For “quasi longitudinal” in figure (E), only the E_1 character at 581cm^{-1} can be seen and because of its weak intensity and line shape, no conclusive frequency shift can be determined.

To observe A_1-LO, the longitudinal phonon has to polarize along the z axis. As we can see in figure (G), incoming and scattered light propagate and are polarized in the xy plane, the E_1 longitudinal should be observed for phonon propagation along the x axis and the A_1-LO along the z axis. Because of the relatively weak E_1 component, the E_1-LO phonon was not observed, but the A_1-LO is well resolved at 574cm^{-1}.

Also two lines are found at 101cm^{-1} and 437cm^{-1} which clearly related to E_2 vibrations. They appear with large intensities in x(yy)z, and x(yx)z directions and are missing in all zz and xz directions.[61, 62]

In general there isn’t any significant differences between the thin film and bulk ZnO, just a small redshift of the LO mode frequencies of the ZnO films with respect to the bulk material was probably assigned to the existence of the vacancy point defects within the films. At table 3.1 a range of observed Raman shifts for wurtzite ZnO is shown.[20, 61, 62]

Table 3.1: Raman shifts for wurtzite ZnO

Symmetry	**Raman shifts (Cm^{-1})**
A_1 – TO	378 – 380
E_1 – TO	407 – 413
A_1 – LO	574 – 579
E_1 – LO	583 – 591
E_2 – low	98 – 102
E_2 – high	437 – 444

At figure 3.4, the phonon - dispersion relations and one-phonon DOS (Densities of States) of ZnO is shown; on the right hand of the plot, the solid curves represent the one - phonon DOS, whereas dashed and dotted curves display the projected DOS corresponding to zinc and oxygen displacements respectively. The diamonds in the figure stand for Raman data and we can see the relation of DOS and Raman data.[63]

Also there are some well resolved multi-phonon processes, peaks around 205cm^{-1} related to the 2TA or 2E_2^{low}, 330cm^{-1} related to the E_2^{high} – E_2^{low}, broad band at 540 – 700cm^{-1} related to the optical – acoustical combination, and broad band at 980 – 1200cm^{-1} related to the optical combination. Serrano *et al.* calculated all of the two-phonon DOS and compared them with experimental second order Raman data as shown in table 3.2.[20, 61, 62, 63]

In figure 3.5 the unpolarized Raman spectra of the single crystal of ZnO is shown. In this figure the first order and second order Raman shifts are shown and clarified.

Table 3.2: Comparison of structures in the two-phonon DOS (sum and difference modes) with second order Raman data[63]

Symmetry	Calculations (cm^{-1})	Experiments (cm^{-1})
$2TA_L$	225	205, 208, 213
$LO - B_1$	290	302
$E_2^{high} - E_2^{low}$	348	330 – 334
$[2B_1]_{\Gamma, L, M}$	520	530, 540
$[TA + TO]_{A, L, M}$	590	Overlap with first order
TA + LO	650	675 – 680
B1 + LO	810	800 – 820
$2TO_{A, L, M}$	930	986, 990
$[TO + LO]_{A, L, M}$	1000	1080, 1084
$2LO_{A, L, M}$	1100	1149, 1160
$2LO_{\Gamma}$	1120	1200

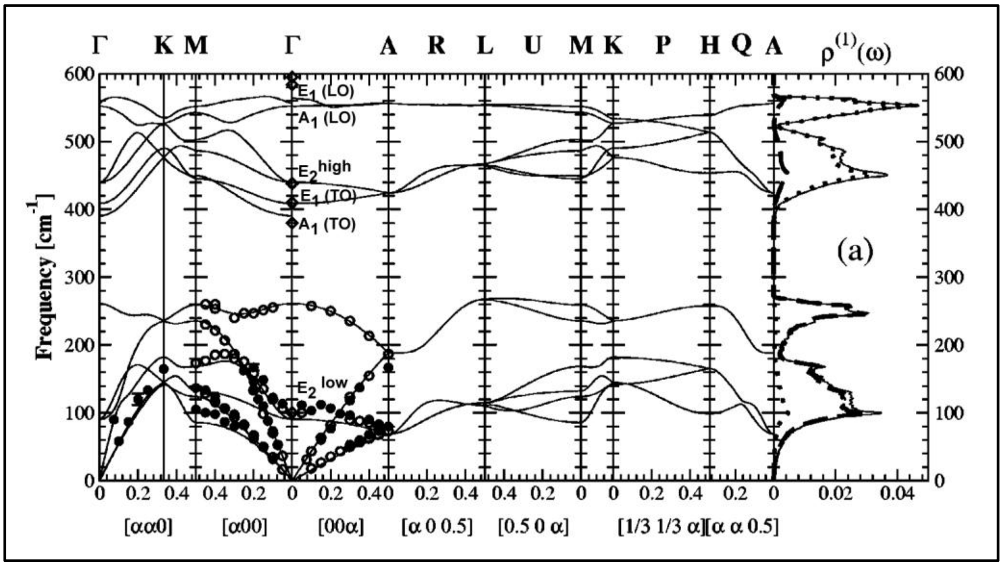

Figure 3.4: phonon-dispersion relations and one-phonon DOS of ZnO and the relation of DOS and Raman data[63]

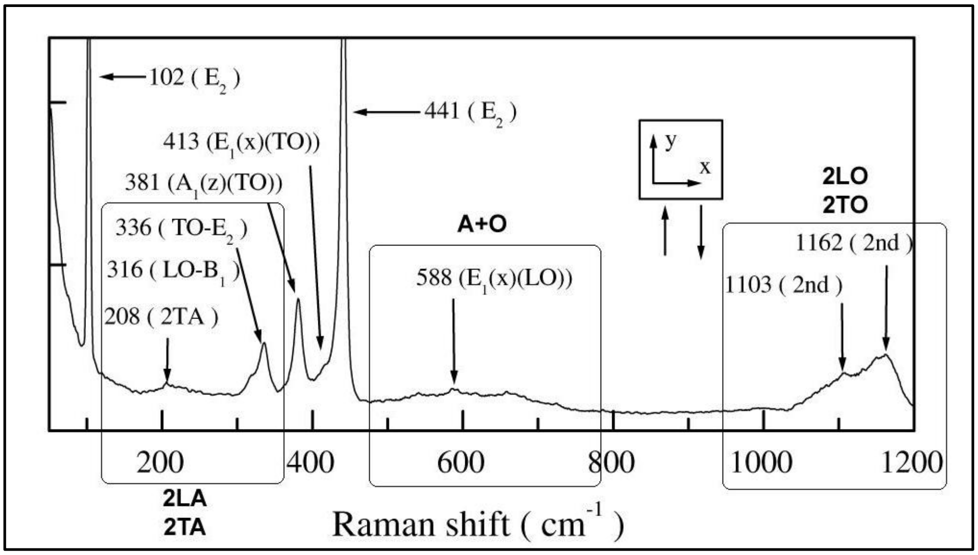

Figure 3.5: Unpolarized Raman spectra of ZnO single crystal[64]

The band gap in ZnO is about 3400 Å, and so a UV laser is required as the excitation source for resonant scattering. In figure 3.6 we can see a resonant Raman scattering of ZnO with 3250 Å excitation. The spectrum consists of a broad luminescence envelope peaking at about 3750 Å (3.31 eV), with relatively sharp lines superimposed upon it. These sharp lies are at frequency shifts which are multiples of the E_1-LO zone-center frequency of 585 cm^{-1}.[65]

Also in 3.7 we can see the pre-resonant Raman scattering with visible excitation of the wurtzitic ZnO. As we can see, nearly constant A_1(TO) height and the strong resonance of the 2LO region. Also it is possible to see a weak resonance in 2LA and 2TA and A+O regions.[62]

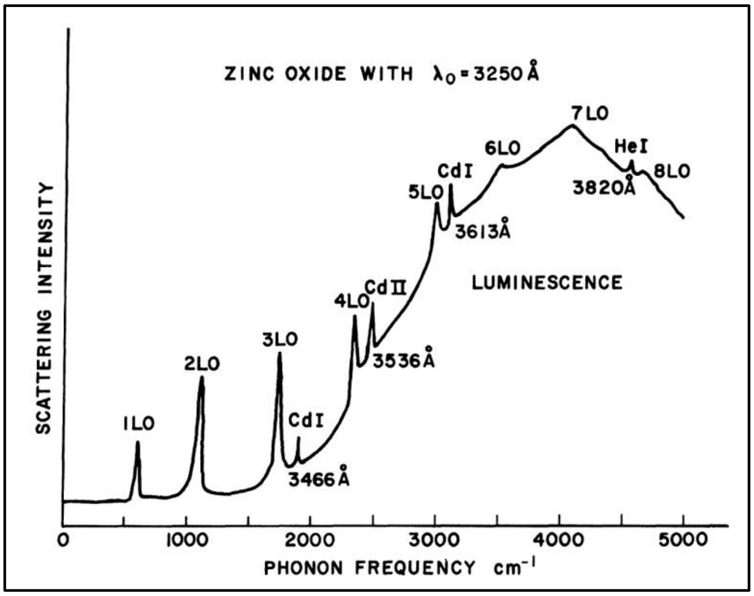

Figure 3.6: Raman Spectrum of ZnO for X(ZX)Y scattering at 295 ^{0}K and 3250 Å excitation[65]

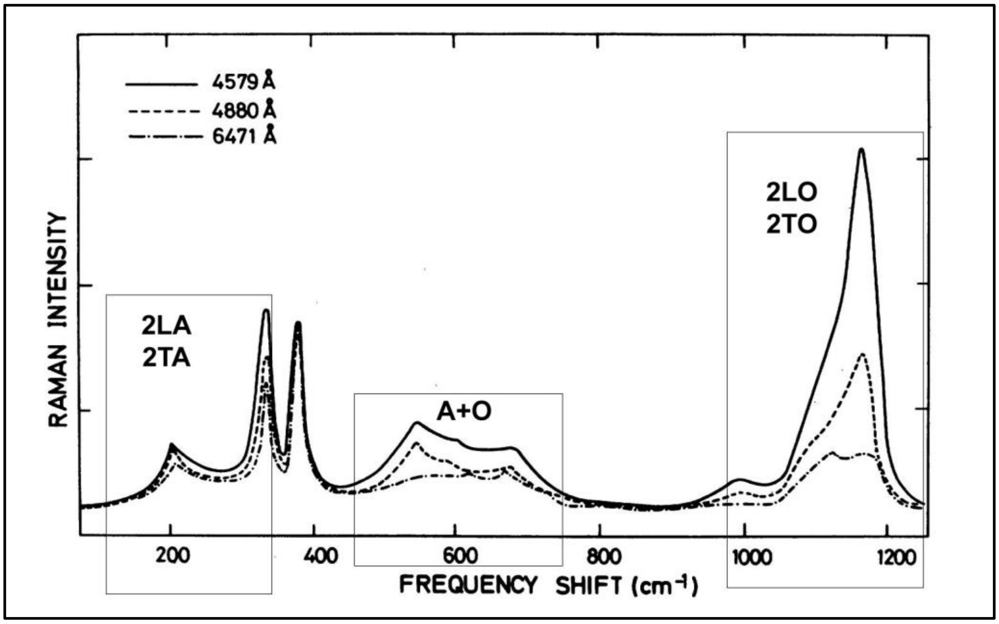

Figure 3.7: Raman spectra recorder for several wavelengths in x(zz)~~x~~[62]

3.3 Raman of AZO

As we said before, recent research interest is focused on doped ZnO to improve electrical conductivity behavior of ZnO via free charge carrier. Raman spectroscopy is a versatile technique for fast and nondestructive study of dopant incorporation, particularly when impurity induced modes can be traced back to individual constituents and their concentration.

As we can see in figure 3.8, Bundesmann *et al.* checked Raman scattering of ZnO thin films doped with Fe, Sb, Al, Ga, and Li and showed some of the additional modes appear only in the spectra of ZnO thin films with certain dopant species, such as 720cm^{-1} for Fe doped, 531cm^{-1} for Sb doped and 631cm^{-1} for Ga doped. These modes seem to be related to the individual dopants and may be used as indication for incorporation of these dopants. Also there are some other additional modes that are related to intrinsic host lattice defects, we can see these modes at 277, 511, 583, 644 cm^{-1} for Fe, Sb, and Al doped films.[66]

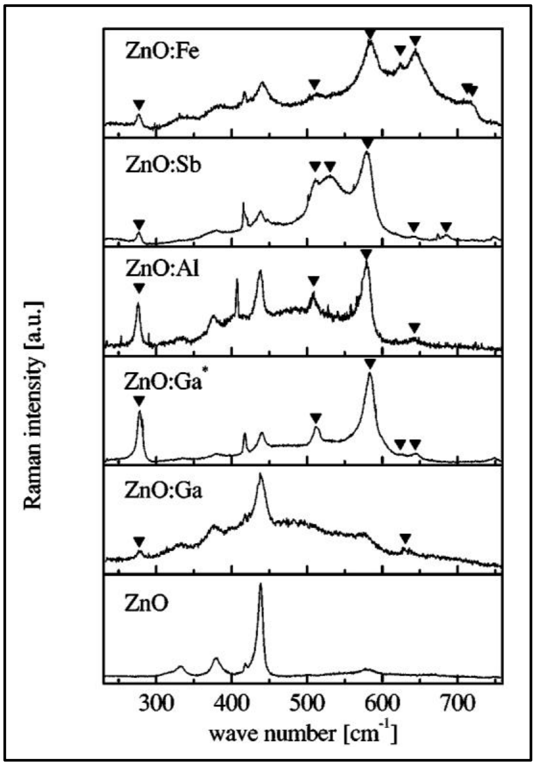

Figure 3.8: Raman scattering of different types of doped ZnO and their additional modes.[66]

Tzolov *et al.* observed electric field induced (EFI) Raman scattering in AZO. EFI Raman scattering leads to LO enhancement and therefore the band at approximately 570cm^{-1} is most intensive in the AZO samples compare to ZnO samples. It was reported that there are silent modes with B_2 symmetry in the spectral range 250 – 300cm^{-1} in the phonon dispersion curves of monocrystalline ZnO. It can be assumed that the observed band at 276cm^{-1} is due to the electric field induced Raman activity of the B_2 modes (figure 3.9 A). Also the addition of oxygen during the deposition process leads to formation of more insulting films and therefore the value of the built-in electric filed decreases. As a result the intensity of LO band decreases with the addition of oxygen (figure 3.9 B).[67]

In general there isn't enough research related to Raman spectroscopy of AZO and exactly there isn't enough work related to the effect of deposition parameters on AZO Raman spectroscopy results.

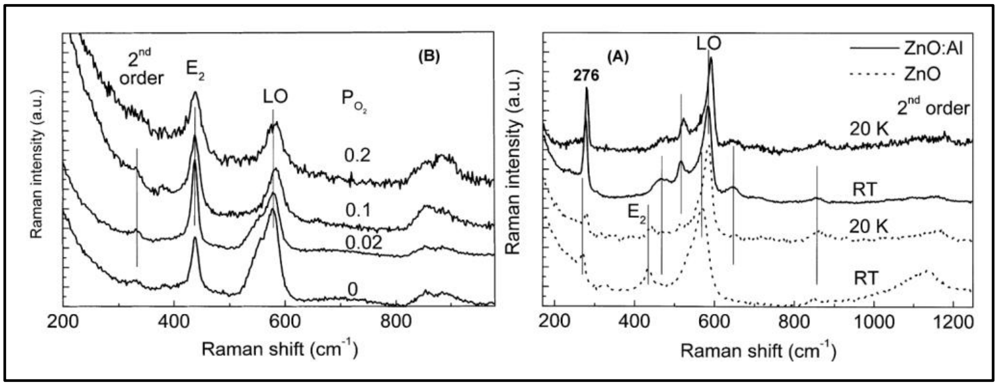

Figure 3.9: A) Raman spectra of ZnO and AZO films at room temperature and 20 K. The intensity of the spectra is normalized and they are vertically shifted for clarity. It is possible to see the B_2 modes at 276cm^{-1}. These films are conductive B) Raman spectra of ZnO films deposited at different oxygen content during deposition. The spectra are vertically shifted for clarity. These films are insulator [67]

Chapter4:

Results and discussion

4.1 Sample description

In this chapter the procedure that was used for preparing samples and also the results that we obtained will be described.

AZO and ZnO were grown by PLD on 4 different types of substrates. AZO samples were grown on these different substrates by ablating an Al_2O_3 (2% wt.):ZnO sintered target with a ns-pulsed laser (Nd:YAG 4th harmonic, $\lambda = 266$ nm, $f_p = 10$ Hz and pulse duration $\approx$ 6 ns). In order to favor film adhesion and to reduce micro particulate, limiting atomistic peening phenomena [38], the laser energy density on the target was reduced to $1 \mathrm{Jcm}^{-2}$. Before the deposition, substrates have been cleaned first by solvents (2-propanol and acetone) and second by ion gun in oxygen plasma. The distance between target and substrate was fixed at 50 mm. For AZO compact films (hereafter defined up to 10 Pa pressure), roughly a 500 nm film thick was obtained after 36 minutes (21600 pulses) of deposition. On the other hand, for AZO porous film (defined starting from a pressure of 100 Pa) the deposition time was fixed at 30 minutes (18000 pulses). The type and pressure of background gas were varied and will be described later. All the depositions were done in room temperature.

Depending on the characterization technique, different substrates have been used:

- Glass (soda-lime) for Raman analysis especially after annealing, XRD and optical measurements.
- Ti for Raman analysis especially for as deposited samples.
- ITO for SEM analysis especially for porous films.
- Si (100) for SEM and electrical analysis.

Raman spectroscopy was performed by Renishaw 150 INVIA spectrometer, the exciting radiation is produced by an argon ion laser (model 150 I-select) of the Laser-Phisics capable of emitting at 514.5, 488 and 457 nm. The laser emits up to 50 mW (figure 4.1). In this thesis Raman spectra were measured by spectral resolution 3cm^{-1} with two wavelengths, 514.5 nm and 457 nm, and 1mW power. SEM measurements were performed by Zeiss SUPRA 40 field-emission SEM. Depositions of the samples were done by a collaboration with a Ph.D. student.

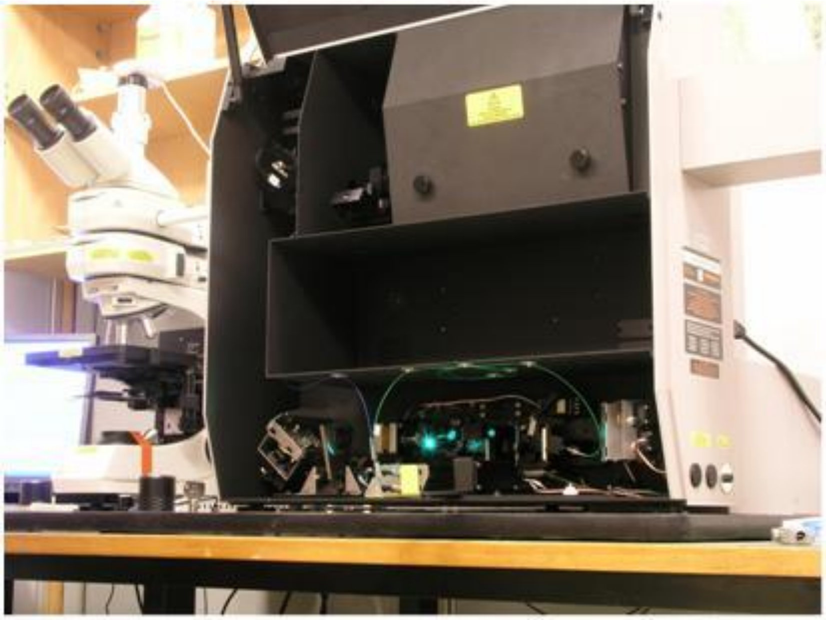

Figure 4.1: Raman spectrometer were used in this thesis.

Totally 4 different types of samples were deposited and compared.

- ZnO samples deposited in different oxygen pressure, from 0.01Pa to 100Pa. These samples were compared with AZO samples and the effects of aluminum doping in the Raman spectra and structure were checked.

- AZO samples deposited in different oxygen pressure, from 0.01Pa to 100Pa. These samples were compared related to different oxygen pressure and also after 6 months aging.

- AZO samples deposited in mixed atmosphere of oxygen and argon. These samples were compared related to different ratio of oxygen and argon.
- AZO samples annealed in vacuum and argon atmosphere in 350°C and 500°C, then the effect of annealing was checked.

Each of these 4 different types will be discussed in the next parts.

4.2 ZnO

At first ZnO samples were deposited in 4 different oxygen pressure, 0.01, 2, 10, and 100Pa; then by comparison of ZnO samples and AZO samples in next part, the effect of aluminum doping in Raman spectra was checked.

Raman spectra of these samples were measured with 457nm and 514.5nm excitation. At the end of the next part, these Raman spectra were compared with Raman spectra of AZO samples deposited exactly at the same oxygen pressure.

In figures 4.2 to 4.5, it is possible to see in SEM figures, with increasing deposition pressure from 0.01Pa to 100Pa the morphology changes from completely compact to almost compact. These compact films show a columnar structure with the axis normally oriented to the surface reflecting the ZnO wurtzite lattice structure.

As we can see in Raman spectra of these samples, with introducing more oxygen, the peak at 437cm^{-1} related to E_2^{high} mode is more intense and the LO band shift from 564cm^{-1} to 580cm^{-1}. This E_2^{high} mode according to literature is related to vibration of only oxygen atoms.[20] At lower oxygen pressure, zinc excess caused resonance effects for LO modes in the visible range due to the presence of impurity states. This resonance effect is more noticeable in Raman spectra with 457nm excitation.

Also we can see another peak around 330cm^{-1} in samples deposited in 10 and 100Pa of oxygen, this peak appeared when we have more oxygen pressure and more intense E_2^{high}; one of the interpretation of this peak according to literature[20, 63] is related to $E_2^{high} – E_2^{low}$ multi phonon process. Aluminum induces disorder and this second order peak is less evident; with blue excitation (457nm) related to pre-resonant Raman scattering intensity is larger.

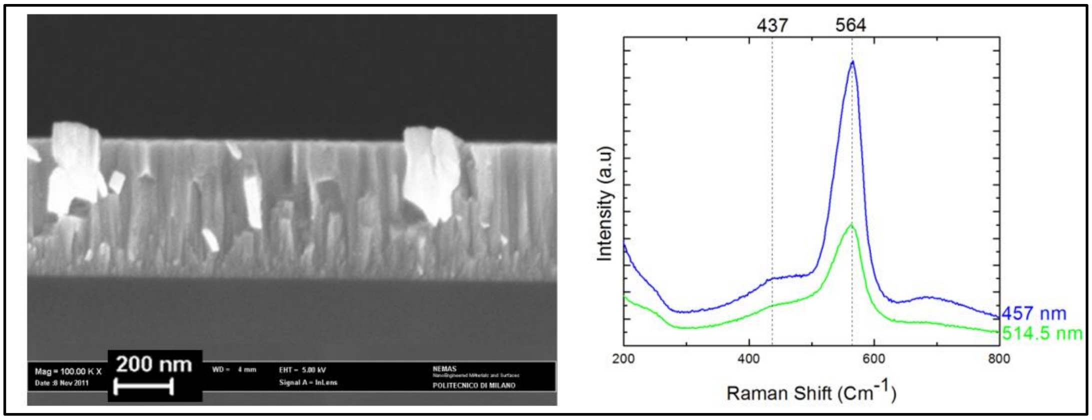

Figure 4.2: SEM and Raman spectra of ZnO samples deposited in 0.01Pa of oxygen

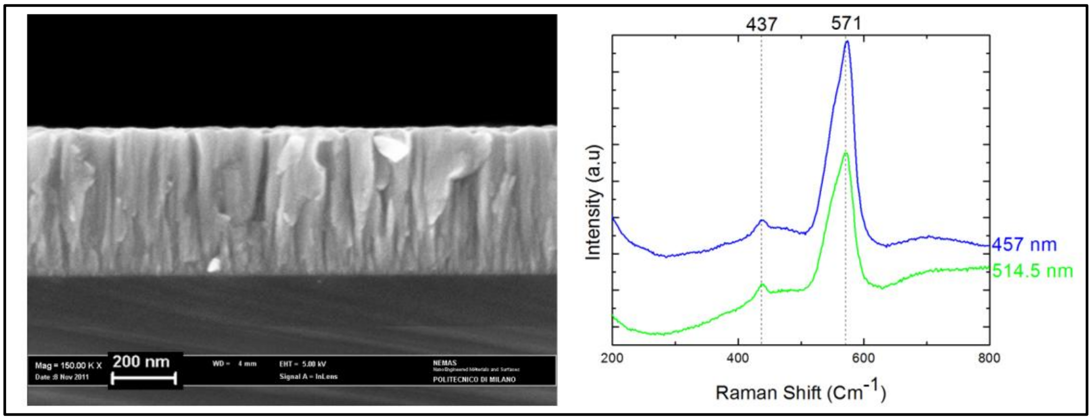

Figure 4.3: SEM and Raman spectra of ZnO samples deposited in 2Pa of oxygen

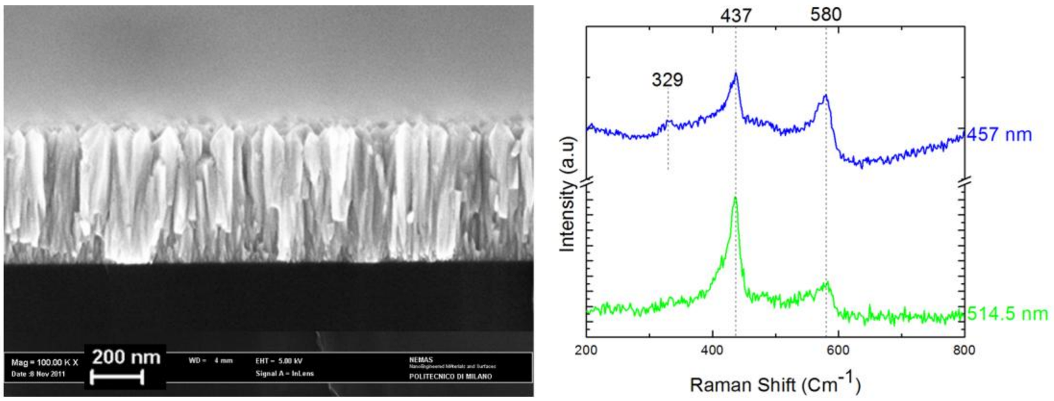

Figure 4.4: SEM and Raman spectra of ZnO samples deposited in 10Pa of oxygen

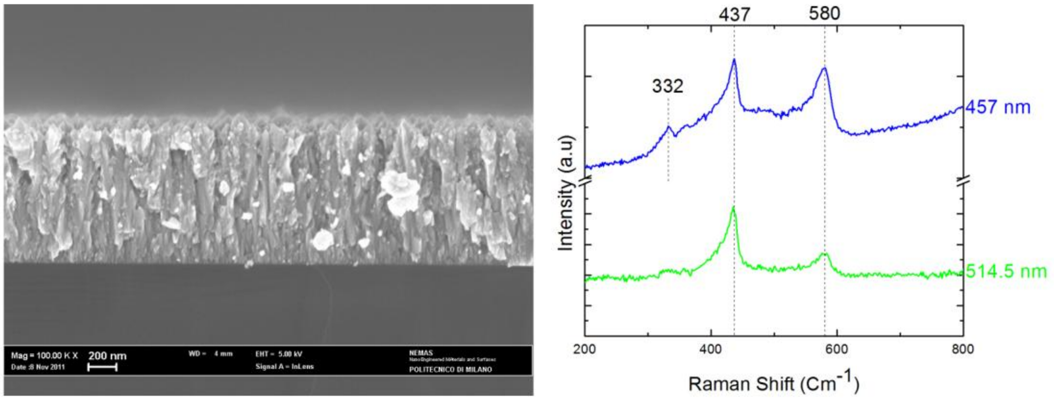

Figure 4.5: SEM and Raman spectra of ZnO samples deposited in 100Pa of oxygen

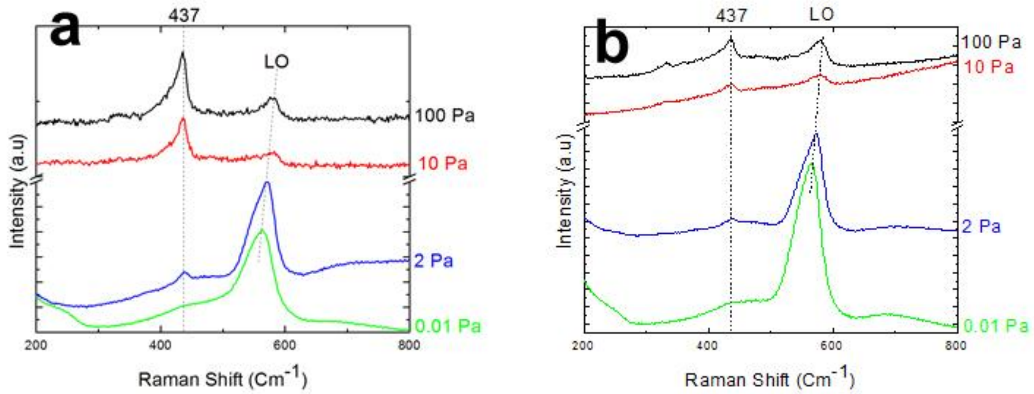

Figure 4.6: Raman spectra of ZnO samples deposited in different oxygen pressure. a) 514.5nm excitation b) 457nm excitation

As we can see in figure 4.6, with increasing oxygen pressure, the intensity of LO band reduces and it goes to higher wave number and the intensity of E_2^{high} at $437cm^{-1}$ increases.

4.3 AZO samples deposited in pure oxygen

These samples were deposited in different pressure of pure oxygen; 0.01, 0.1, 1, 2, 10, 50, 70, 80, 100, 160, 180, and 200Pa. Related to the morphology of samples, they were divided in three groups: from 0.01Pa to 10Pa are described as compact samples, from 50Pa to 80Pa are described as intermediate samples, and from 100Pa to 200Pa are described as porous samples.

It is possible to see in SEM figures (figure 4.7 to 4.18), with increasing deposition pressure from 0.01Pa to 200Pa the morphology changes from compact to porous. According with the literature results [7]. AZO compact films deposited in 0.01 and 0.1Pa of oxygen shows amorphous structure as shown in figures 4.7 and 4.8, but AZO compact films with higher oxygen pressure show a columnar structure with the axis normally oriented to the surface reflecting the ZnO wurtzite lattice structure as shown in figures 4.9 to 4.11. In figures 4.12 to 4.14 it is possible to see the AZO intermediate films were growth at the pressure 50, 70, 80Pa. These intermediate films as we can see, neither have columnar structure same as compact films, nor have nanostructures same as porous films. In figures 4.15 to 4.18 it is possible to see the AZO nanostructured porous film were growth at the oxygen pressures of 100, 160, 180 and 200Pa. These tree-like morphologies is almost something new in the literature for AZO films, and AZO porous films lost the oriented columnar structure typical of the compact films. By fixing the deposition time, the film thickness depends on the background gas pressure arriving up to 4.1µm at 200Pa of oxygen pressure. This fact is in contrast with compact films, where the film thickness is roughly constant (average values of 500nm) with the pressure.

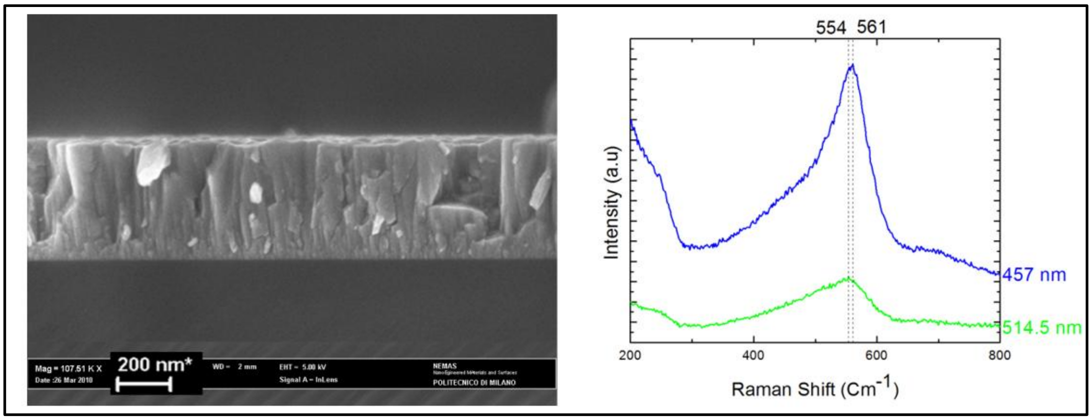

Figure 4.7: SEM and Raman spectra of samples deposited in 0.01Pa of oxygen

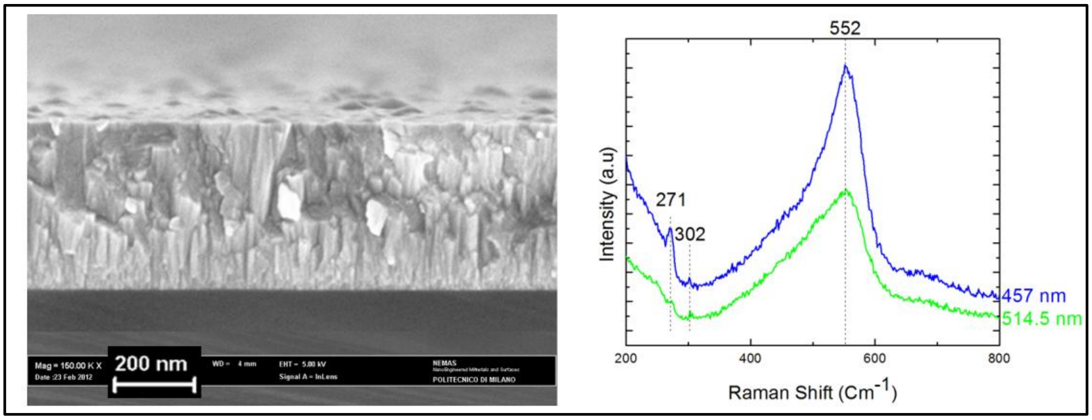

Figure 4.8: SEM and Raman spectra of samples deposited in 0.1Pa of oxygen

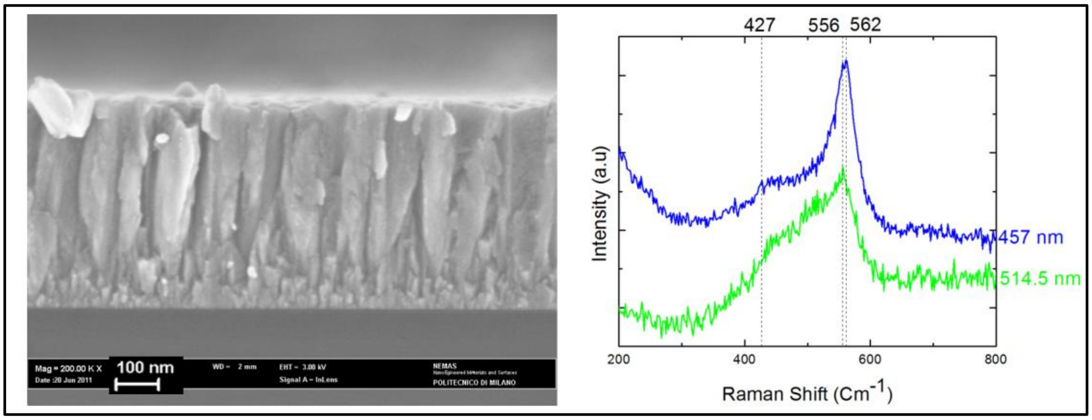

Figure 4.9: SEM and Raman spectra of samples deposited in 1Pa of oxygen

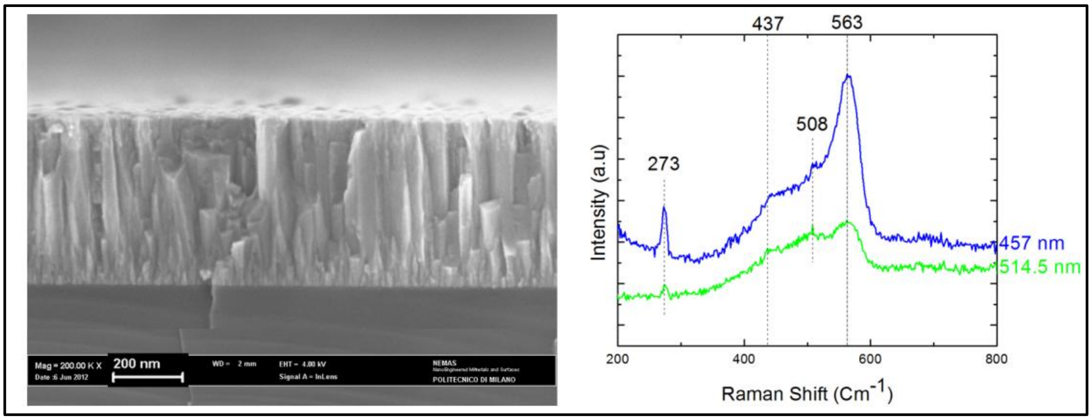

Figure 4.10: SEM and Raman spectra of samples deposited in 2Pa of oxygen

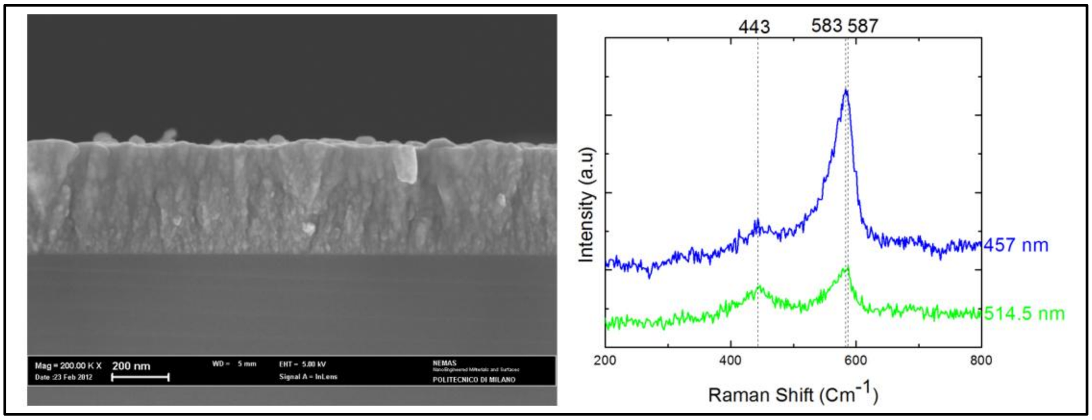

Figure 4.11: SEM and Raman spectra of samples deposited in 10Pa of oxygen

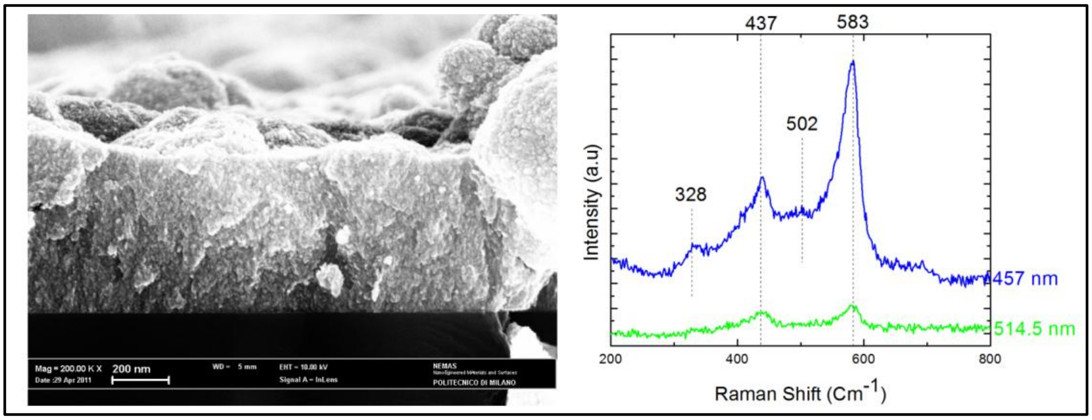

Figure 4.12: SEM and Raman spectra of samples deposited in 50Pa of oxygen

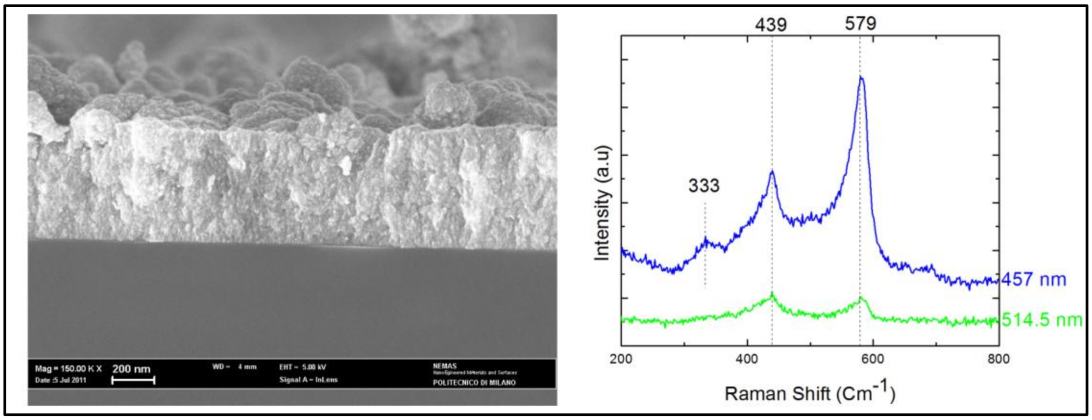

Figure 4.13: SEM and Raman spectra of samples deposited in 70Pa of oxygen

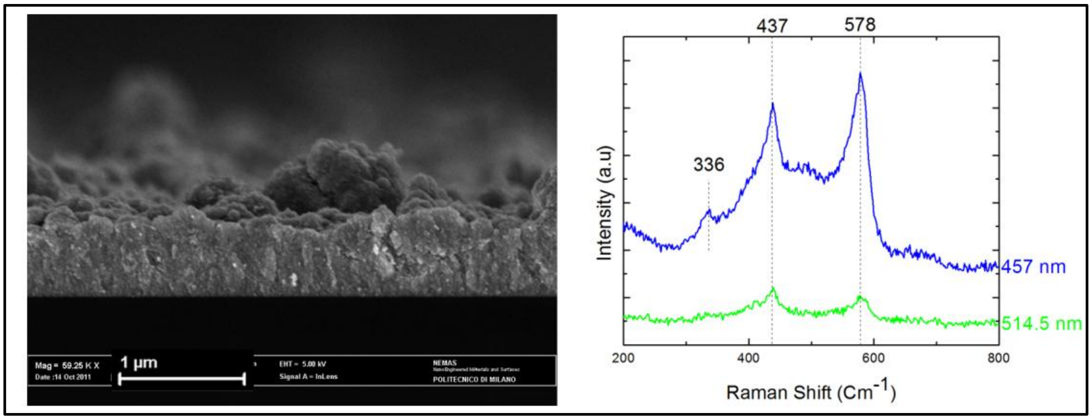

Figure 4.14: SEM and Raman spectra of samples deposited in 80Pa of oxygen

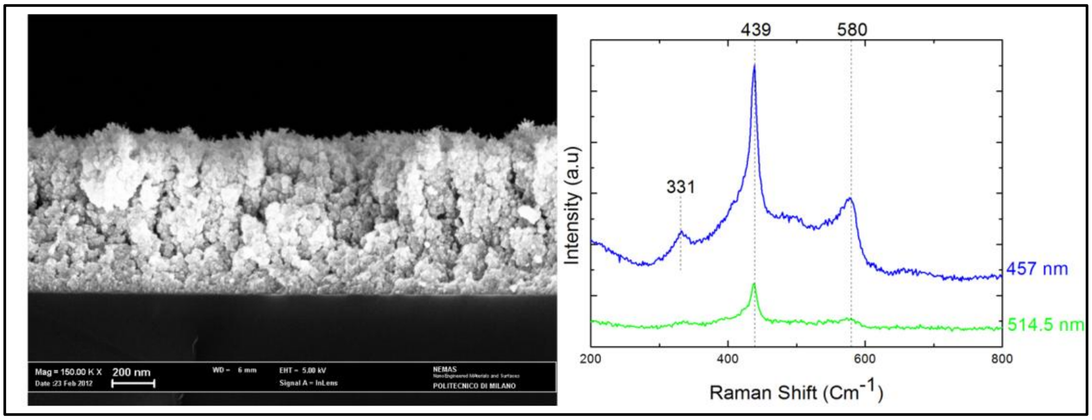

Figure 4.15: SEM and Raman spectra of samples deposited in 100Pa of oxygen

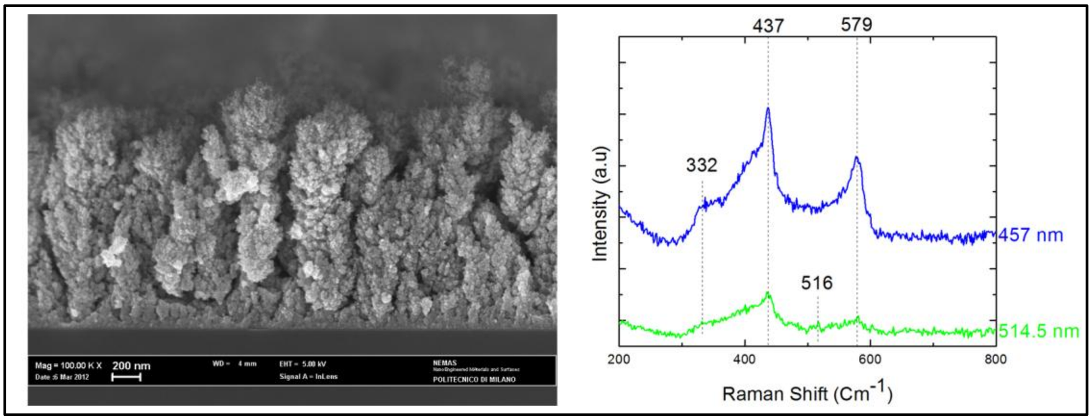

Figure 4.16: SEM and Raman spectra of samples deposited in 160Pa of oxygen

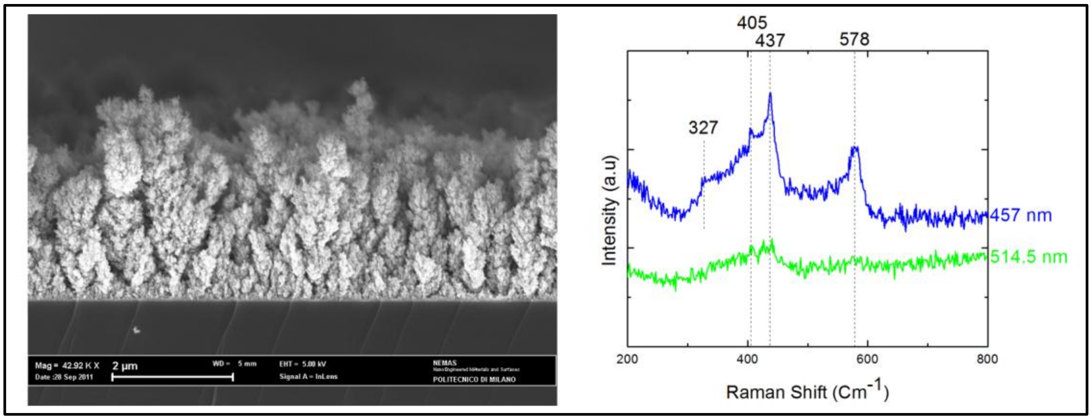

Figure 4.17: SEM and Raman spectra of samples deposited in 180Pa of oxygen

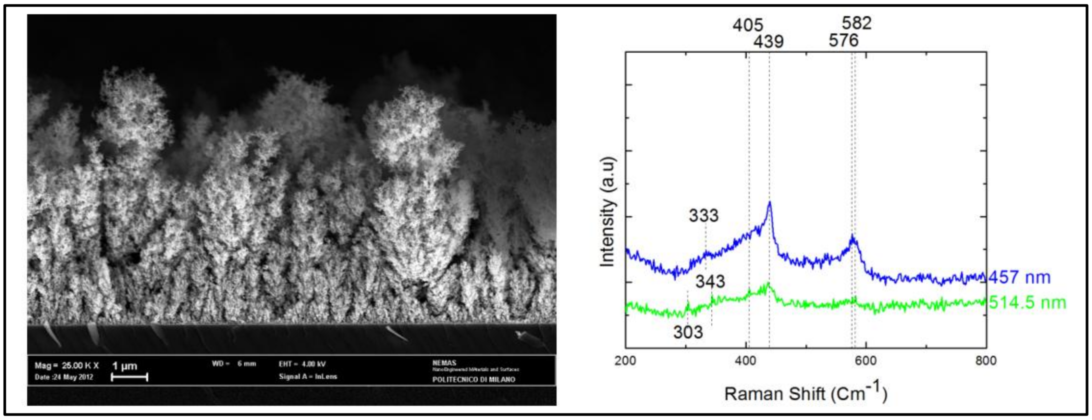

Figure 4.18: SEM and Raman spectra of samples deposited in 200Pa of oxygen

In Raman spectra of compact samples that were deposited on titanium substrate, it is possible to see a band at around 552cm^{-1} – 587cm^{-1}. This band is related to the combination of LO modes. It is possible to see the reduction of intensity of this band with increasing the oxygen pressure. This matter is related to reduction of defects and disorders related to the oxygen stoichiometry and reduction of the zinc excess. Also it is possible to see the introducing the E_2^{high} peak at around 437cm^{-1} with increasing oxygen pressure, this peak is dominant in samples deposited with more than 80Pa of oxygen. As we said before this peak is related to vibration of only oxygen atoms.

Also we can see another peak around 333cm^{-1} in intermediate and porous samples deposited with more than 10Pa of oxygen, this peak appeared when we have more oxygen pressure and more intense E_2^{high}; as we said before according to literature[20, 63] one of the interpretation of this peak is related to $E_2^{high} – E_2^{low}$ multi phonon process. In ZnO samples we saw this peak also in samples deposited with 10Pa of oxygen, this matter can show to us, with introducing aluminum this peak appeared in samples deposited at higher oxygen pressure.

We can see another two peaks in some of the samples, according to literature[63, 67] one of the interpretation of the peak at around 271cm^{-1} is related to B_2 silent mode, and the peak at around 302cm^{-1} is related to the LO – B_1 multi phonon process peak, and the peak at around 510cm^{-1} is related to surface phonon mode (SPMs). Presence of aluminum doping induced activity of B modes and surface phonon modes and as result we can see these additional peaks in Raman spectra.

In samples deposited in 180 and 200Pa of oxygen, we can see a peak at around 405cm^{-1}, this peak according to literature[61] is related to E_1(TO), appearing as a shoulder of the 437cm^{-1} (E_2^{high}), but because of the relatively weak intensity, it is impossible to see this peak in most of the cases.

In comparison between Raman spectra with 514.5nm and 457nm, we can see the pre-resonant effect with 457nm excitation according to literature.[62] This effect is really obvious for LO band.

In general Raman spectra of samples deposited with 2Pa of oxygen or less pressure are same as Raman spectra of conductive films in literature and Raman spectra of sample deposited with 10Pa of oxygen or higher pressure are same as Raman spectra of insulating films according to literature.[67] (see figure 3.9 a and b)

In figure 4.19 we can see a comparison between Raman spectra of AZO and ZnO samples in 4 different oxygen pressures. As we can see, in the case of low oxygen pressure, LO band and E_2^{high} in ZnO is more intense than AZO. This matter can related to introduce of defects with presence of aluminum, this defects caused the reduction of intensity of E_2^{high} mode. In ZnO samples, the intensity of LO band is dominant until 10Pa of oxygen, but in AZO samples, it is dominant until 100Pa of oxygen; this fact also shows introducing aluminum causes defects and reduces the effect of increasing oxygen pressure.

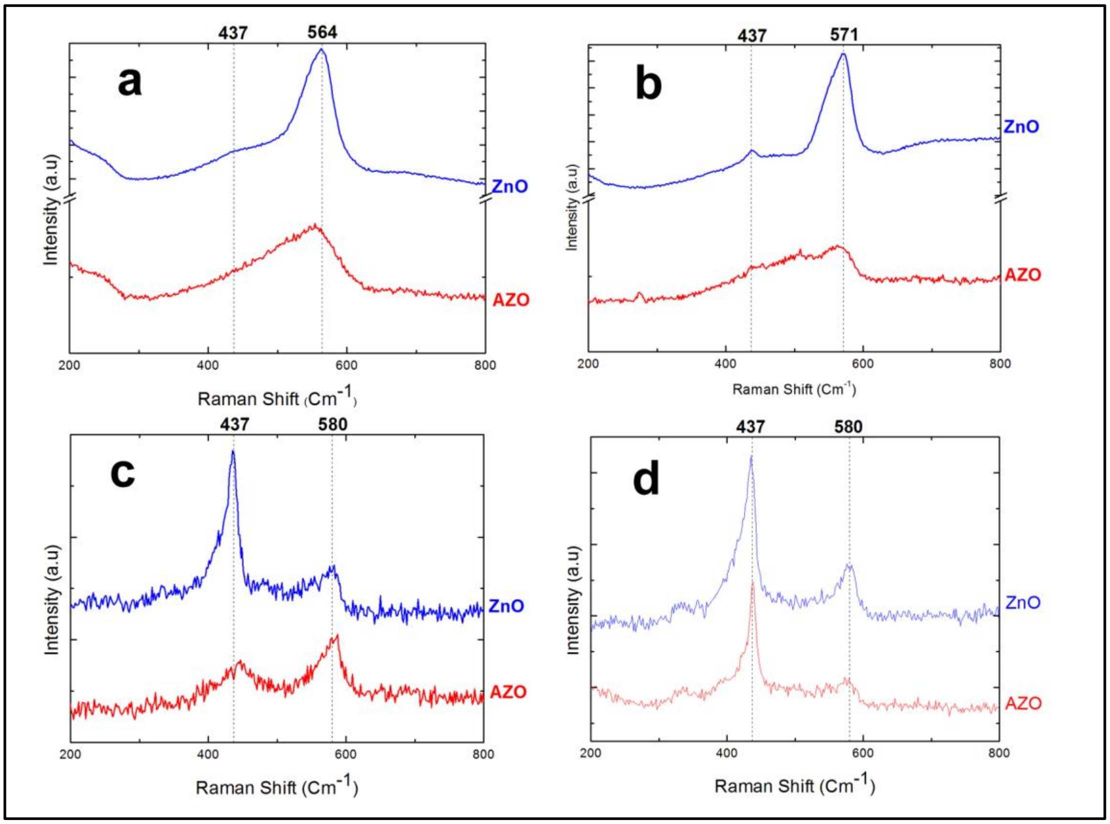

Figure 4.19: Raman spectra of ZnO samples compared with AZO samples at different oxygen pressure with 514.5 nm excitation. a)0.01Pa b)2Pa c)10Pa d)100Pa

4.4 AZO samples after aging

AZO samples were deposited at 0.01, 0.1, 1, 3, 10, 100, 160, and 200Pa in pure oxygen. Raman spectra of these samples were measured as deposition and after 6 months. These Raman spectra compared and the effects of aging on these samples were studied.

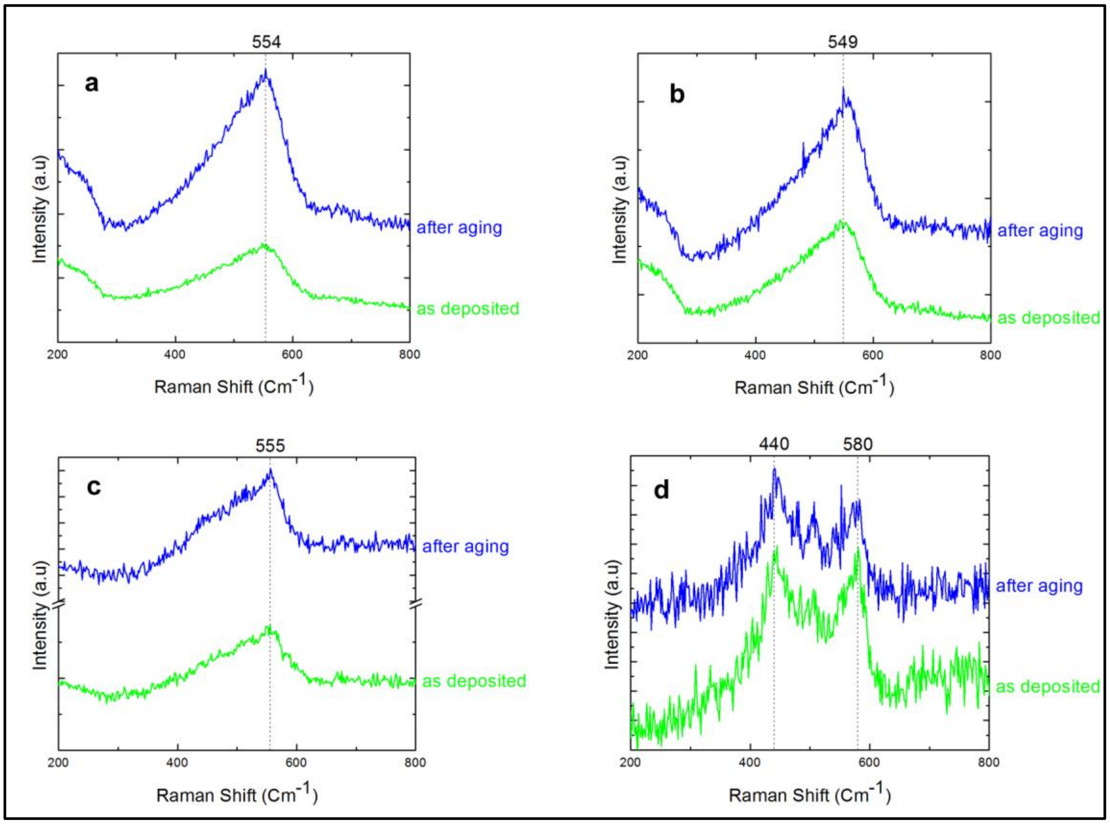

Figure 4.20: Raman spectra with 514.5 nm excitation of AZO samples deposited in different oxygen pressure, before and after aging. a)0.01Pa b)0.1Pa c)1Pa d)10Pa

In figure 4.20 and 4.21 we can see the Raman spectra of compact samples before and after aging with 514.5nm and 457nm excitation. As we can see in figure 4.20 and 4.21, there isn't any significant change in Raman spectra of compact samples after 6 month of aging. In Raman spectra of samples after aging, same as Raman spectra of samples without any aging, we can see LO band and with increasing oxygen pressure, E_2^{high} at around 437cm^{-1}.

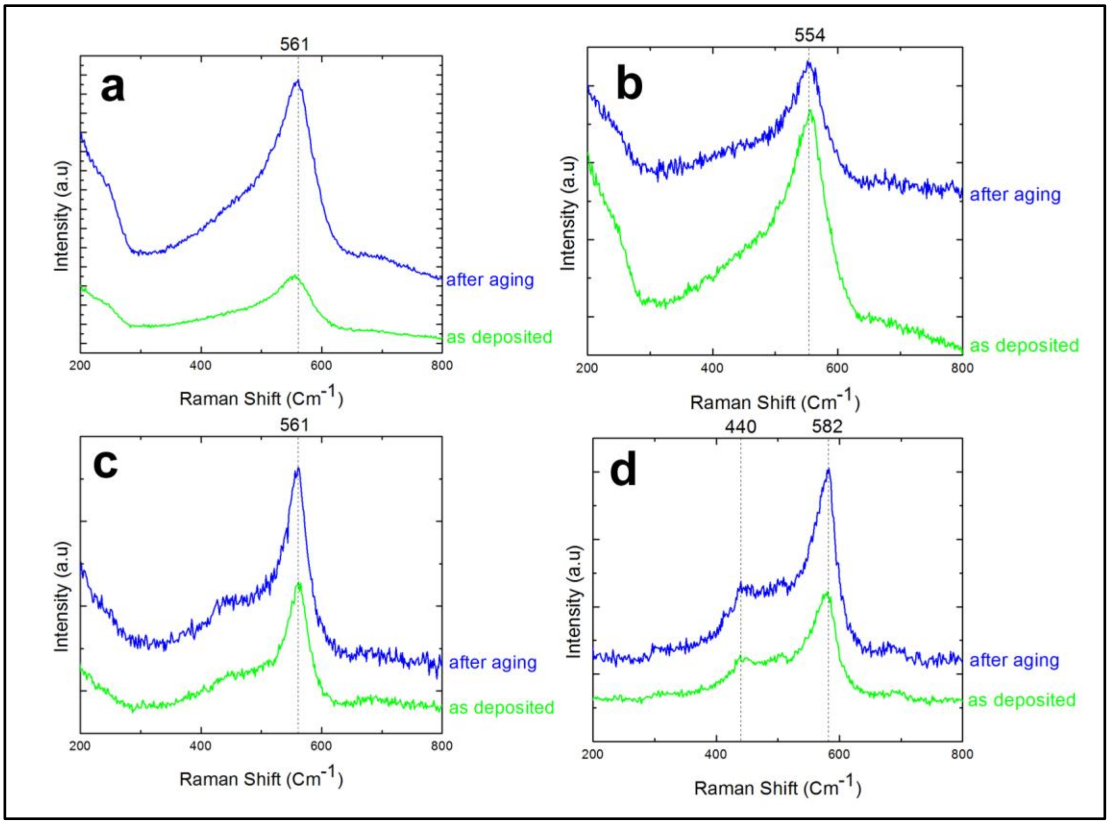

Figure 4.21: Raman spectra with 457 nm excitation of AZO samples deposited in different oxygen pressure, before and after aging. a)0.01Pa b)0.1Pa c)1Pa d)10Pa

In figure 4.22 and 4.23 we can see the Raman spectra of porous samples before and after aging with 514.5nm and 457nm excitation. In porous samples, the peak at 438cm^{-1} is more intense after aging. As we know this peak is related to E_2^{high} mode and it is related to vibration of only oxygen atoms. This increasing in the intensity of this peak shows the reduction of defects during aging in porous samples. These samples have open structure and probably the oxygen atoms can move easily and released stress. As result, we can say in these samples related to the open structure, we have some recrystallization, but in compact samples diffusion and movement of oxygen atoms are difficult and we can't see any significant change.

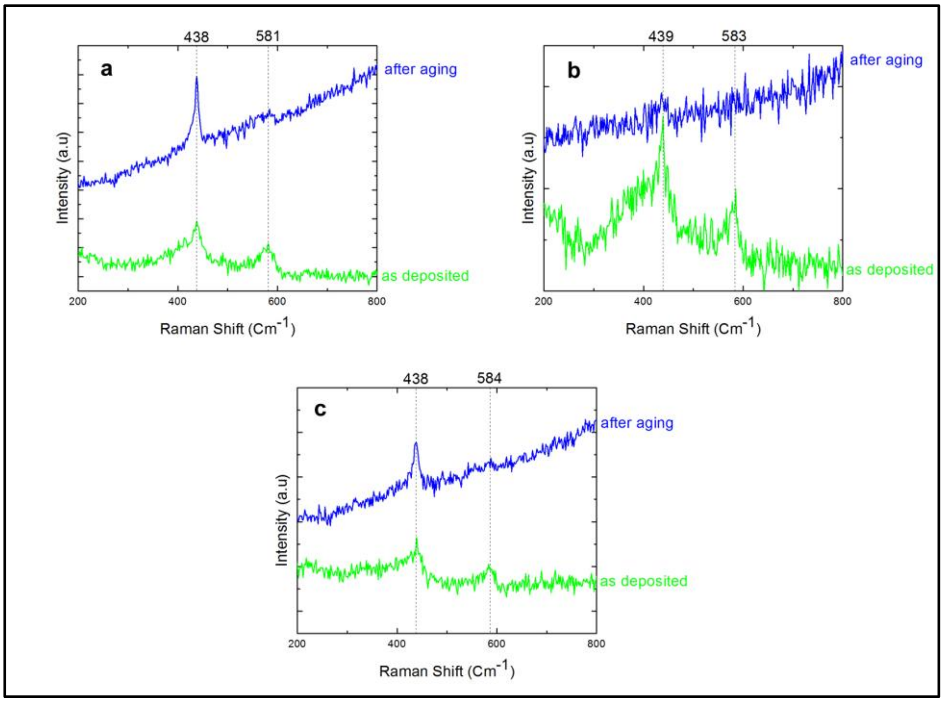

Figure 4.22: Raman spectra with 514.5 nm excitation of AZO samples deposited in different oxygen pressure, before and after aging. a)100Pa b)160Pa c)200Pa

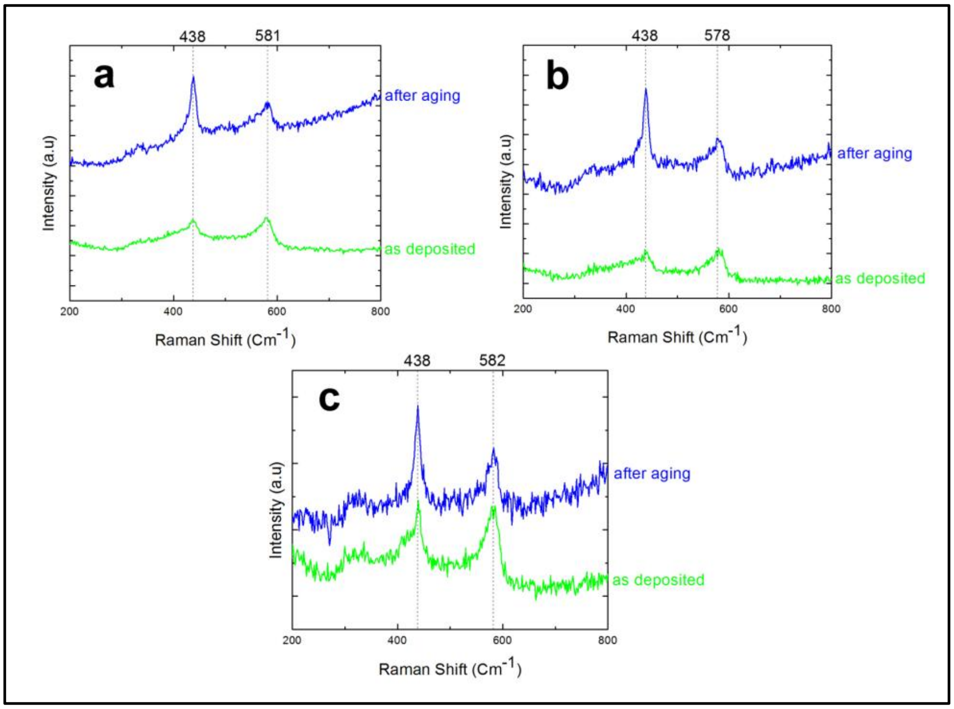

Figure 4.23: Raman spectra with 457 nm excitation of AZO samples deposited in different oxygen pressure, before and after aging. a)100Pa b)160Pa c)200Pa

4.5 AZO samples deposited in mixed atmosphere

These samples were deposited in mixed atmosphere of oxygen and argon. First group of samples were deposited in total pressure of 100 Pa with 0, 2, 5, 10, 50 and 100Pa of oxygen and the remaining part of argon. The second group of samples was deposited in total pressure of 80 Pa with 0, 2, 8, 40 and 80 Pa of oxygen and the rest of argon.

In figures 4.24 to 4.25, SEM and Raman spectra with 457nm (blue wavelength excitation) and 514.5nm (green wavelength excitation) of samples deposited with a total pressure of 100Pa are shown.

It is possible to see in SEM figures (figures 4.24 to 4.29) with increasing oxygen partial pressure from 0 to 100Pa the morphology changes from compact to porous, but morphologies are not exactly the same as with pure oxygen at the same pressure, what is most important for morphology is total pressure. With 2 or 10 Pa of pure oxygen (figures 4.10 and 4.11) is possible to see columnar structures but here in mixed atmosphere, type of structures is same as pure oxygen with higher pressure such as 100 Pa.

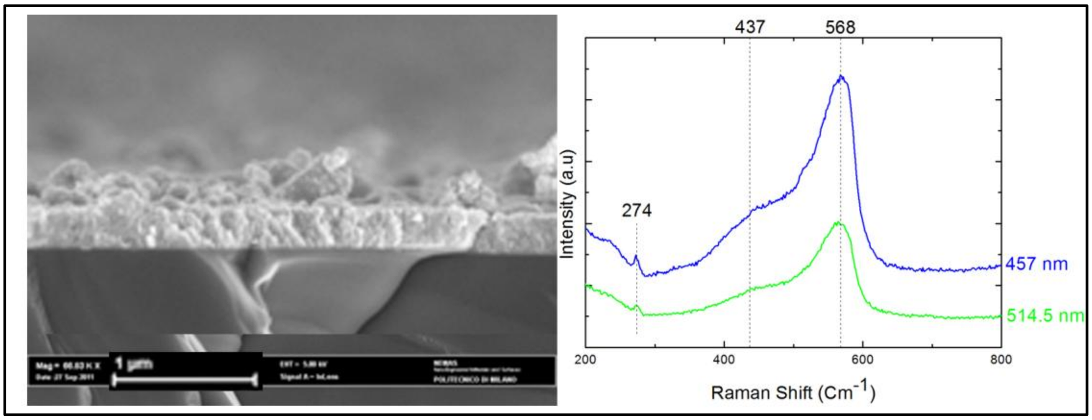

Figure 4.24: SEM and Raman spectra of samples deposited in 100Pa of Argon

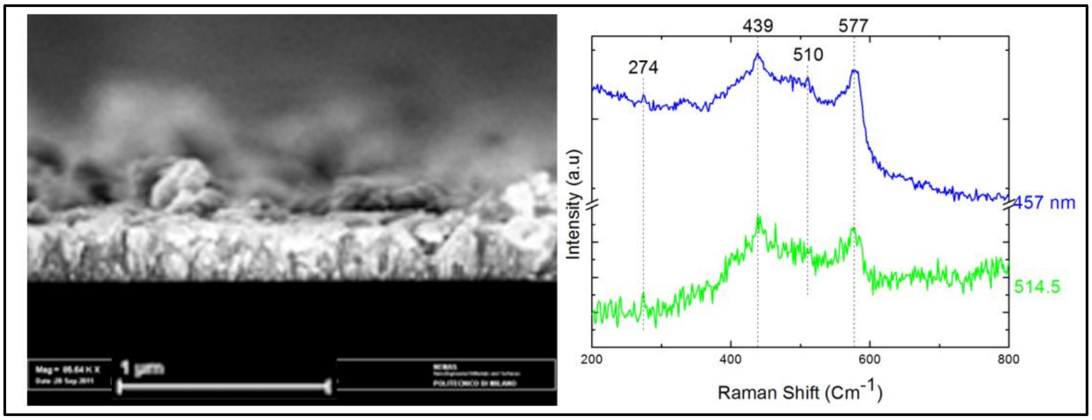

Figure 4.25: SEM and Raman spectra of samples deposited in 2Pa of Oxygen and 98Pa of Argon

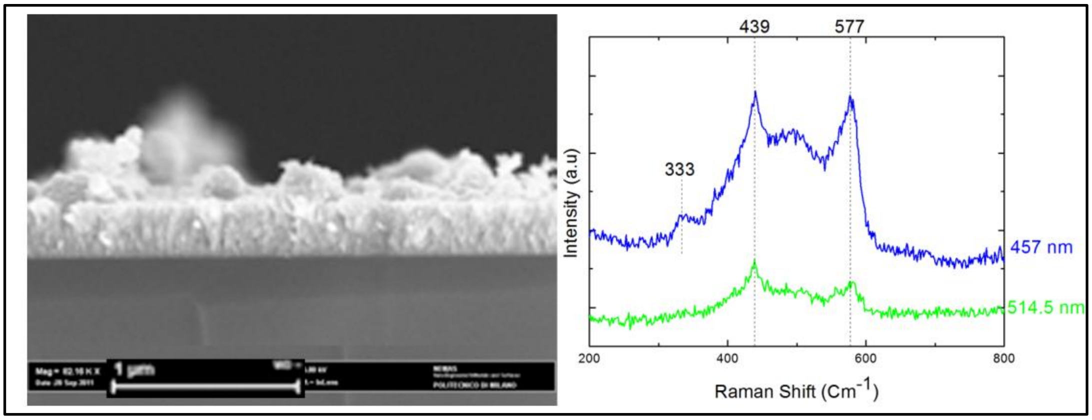

Figure 4.26: SEM and Raman spectra of samples deposited in 5Pa of Oxygen and 95Pa of Argon

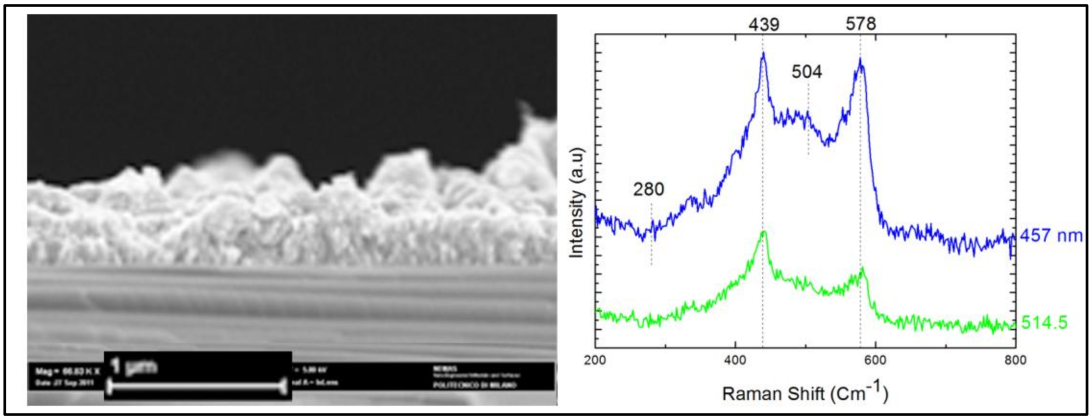

Figure 4.27: SEM and Raman spectra of samples deposited in 10Pa of Oxygen and 90Pa of Argon

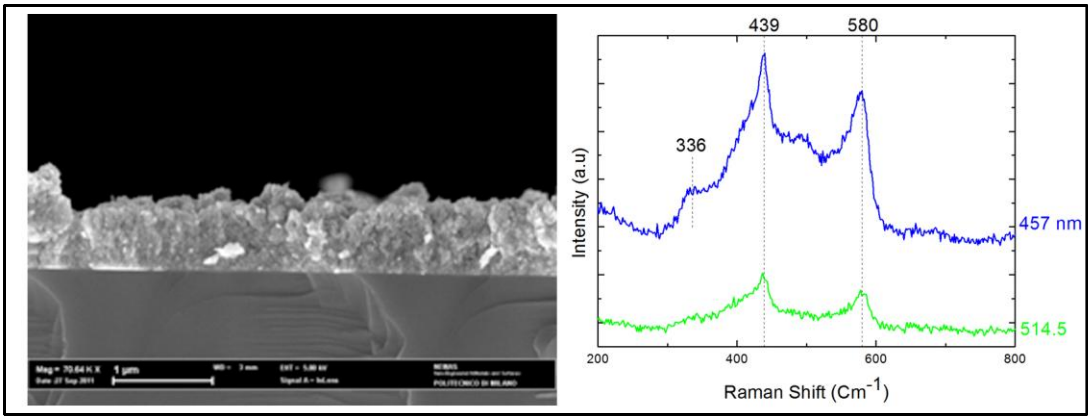

Figure 4.28: SEM and Raman spectra of samples deposited in 50Pa of Oxygen and 50Pa of Argon

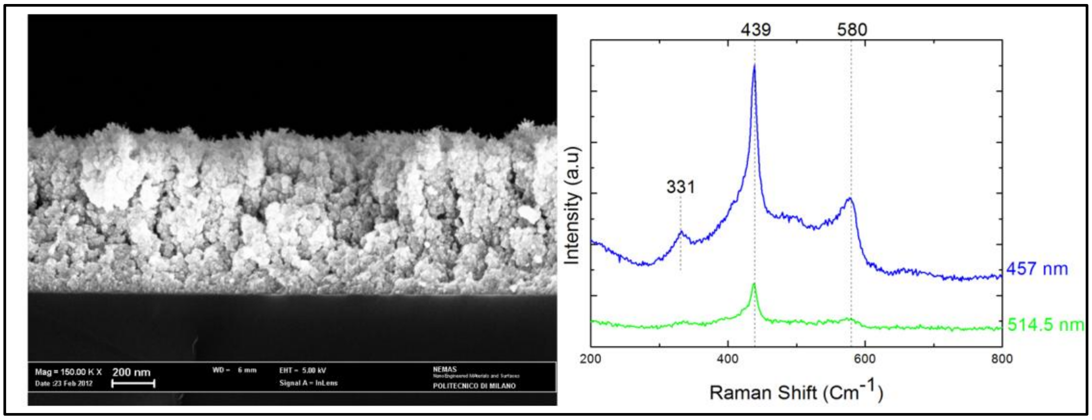

Figure 4.29: SEM and Raman spectra of samples deposited in 100Pa of Oxygen

Raman spectra of these samples were measured by samples that were deposited on titanium. In Raman spectra of the sample deposited in pure argon, it is possible to see a band in the range 564 – 572 cm^{-1}, as we said before this is a LO combination related to A_1(LO) and E_1(LO). Position of this band is changed to 577 – 580 cm^{-1} with the presence of oxygen, in sample without oxygen this band is at 568 cm^{-1}. It is possible to see that the position of this band moves to higher wavenumber with increasing the oxygen pressure.

According to literature[67] one of the interpretation of peaks around 275 cm^{-1} and 510 cm^{-1} are related to aluminum doping effect and the peak appeared around 335 cm^{-1} is related to multi phonon process, this peak is related to $E_2^{high} – E_2^{low}$. The intensity of this peak increased with increasing oxygen partial pressure and increasing intensity of E_2^{high}, as we said before aluminum induces disorder and so this second order peak is less evident; with blue excitation related to the pre-resonant effect intensity of this peak is larger.

Also the peak at 439 cm^{-1} appears with presence of oxygen and will be more intense with increasing the pressure of oxygen and at the same time with increasing the pressure of oxygen the intensity of LO band at 577 – 580 cm^{-1} decrease, this trend is exactly same as the trend of samples deposited in pure oxygen as we discussed in part 4.3. This matter is better shown in figures 4.30 and 4.31. Figure 4.30 and 4.31 are related to Raman spectra with 514.5nm and 457nm excitation of samples with total pressure of 100 Pa and it is possible to see the same trend for both of them. We can see in Raman spectra with 457nm excitation, LO band and E_2^{high} is more intense compare with Raman spectra with 514.5nm excitation, this fact is related to the pre-resonance effect of 457nm excitation.

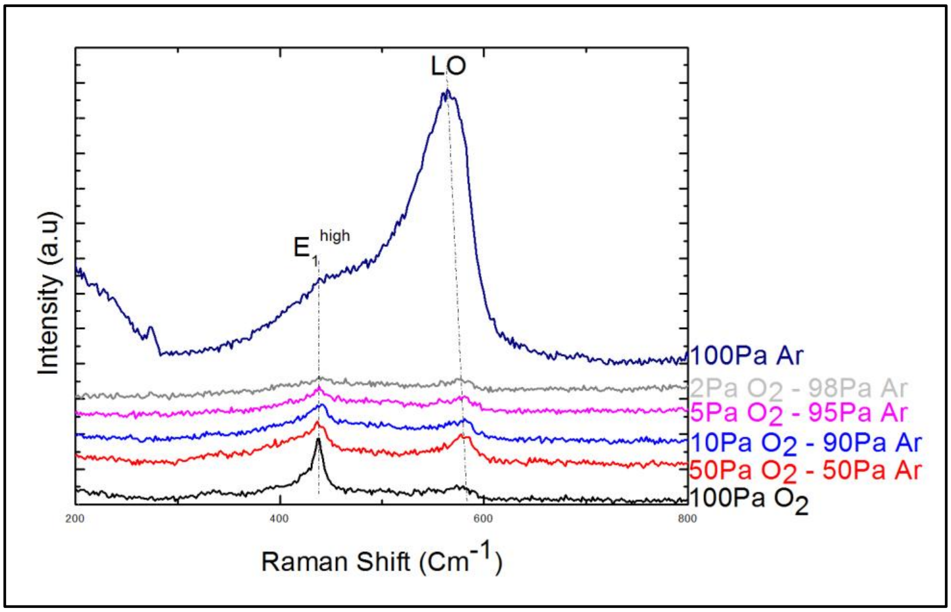

Figure 4.30: Raman spectra with 514.5 nm excitation of samples with mixed atmosphere with total pressure of 100 Pa and different oxygen pressure.

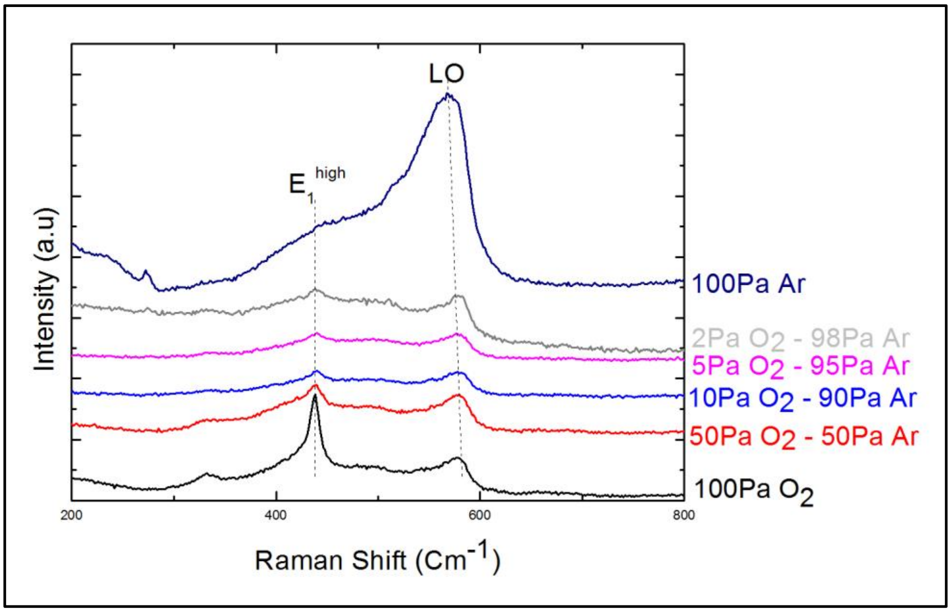

Figure 4.31: Raman spectra with 457 nm excitation of samples with mixed atmosphere with total pressure of 100 Pa and different oxygen pressure.

4.6 Annealing of AZO samples

Two of AZO samples deposited on glass substrate in pure oxygen with 2Pa of oxygen, annealed in vacuum and argon atmosphere in 350°C and 500°C, then the effect of annealing was checked.

For annealing these samples, firstly inside pressure of the chamber was reduced to 10^{-5} Pa. For samples were annealed in vacuum, after this step the vacuum pomp turned off and the output valve was closed and for samples were annealed in argon atmosphere, after reduction the inside pressure of the chamber to 10^{-5} Pa and closing output valve, the argon pumped into the chamber until the inside pressure of the chamber was reached to 10^{5} Pa.

Then the temperature inside the chamber was increased to 350°C and 500°C for both atmosphere types (Argon and vacuum). For the first group of samples, the inside temperature of the chamber was increased from room temperature to 350°C during 45 minutes and then the temperature was kept constant for 1 hour, then the heater was turned off and the chamber temperature decreased to room temperature.

Then the chamber was opened and samples were taken out from the chamber. For the second group of samples the inside temperature of the chamber was increased from room temperature to 500^{o}C during 1hour and then the temperature was kept constant for 1hour, same as first group then the heater turned off and the chamber temperature decreased to room temperature and then samples were taken out.

Raman spectra of these sampled were deposited on glass substrate were measured before and after annealing and the effect of annealing on Raman spectra was studied.

In figures 4.32 and 4.33 the Raman spectra of samples deposited at 2Pa of oxygen on glass substrate and annealed in vacuum at 350^{o}C and 500^{o}C were shown.

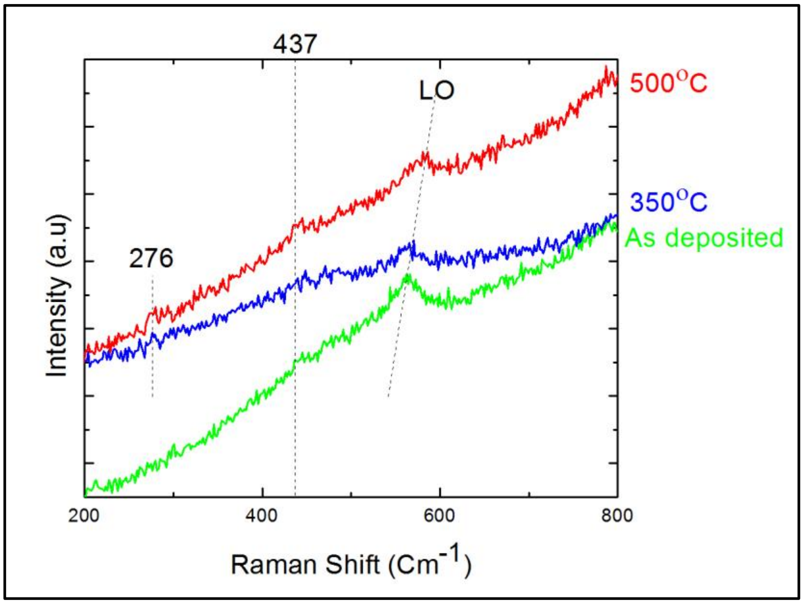

Figure 4.32: Raman spectra with 514.5nm excitation of samples deposited in 2Pa of oxygen and annealed in vacuum at 350^{o}C and 500^{o}C.

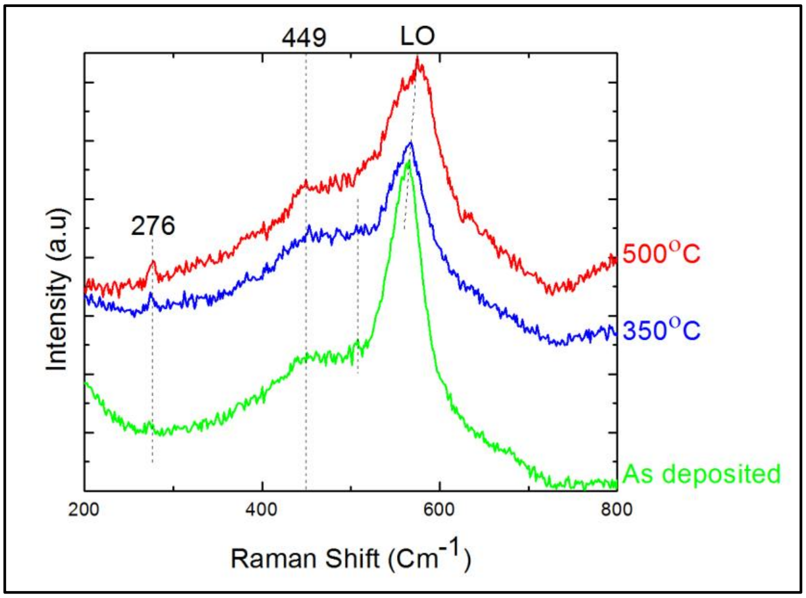

Figure 4.33: Raman spectra with 457nm excitation of samples deposited in 2Pa of oxygen and annealed in vacuum at 350°C and 500°C.

In figure 4.32 the glass substrate leads to high background in Raman spectra, but it is possible to see the LO band goes to higher wavenumber with increasing the annealing temperature, also the intensity of this band decreased with increasing temperature, also in figure 4.33 it is possible to see the same figure. Reduction in the intensity of LO band according to literature is related to the reduction in defects, disorders and oxygen vacancies. At the other hand increasing the annealing temperature leads to increase the intensity of E_2^{high} peak at around $440cm^{-1}$. This effect shows the annealing in vacuum leads the movement of oxygen and zinc atoms, and they leave the inferential positions and go to the vacancies. In general we can see some effects such as reordering the structure and this effect is better shown at higher annealing temperature and higher kinetic energy.

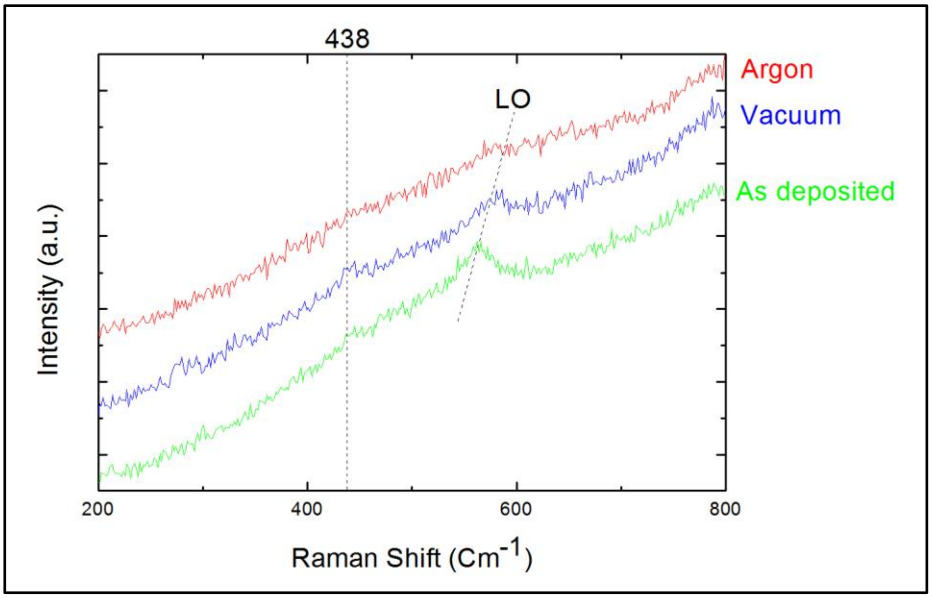

Figure 4.34: Raman spectra with 514.5nm excitation of samples deposited in 2Pa of oxygen and annealed in vacuum and argon at 500°C.

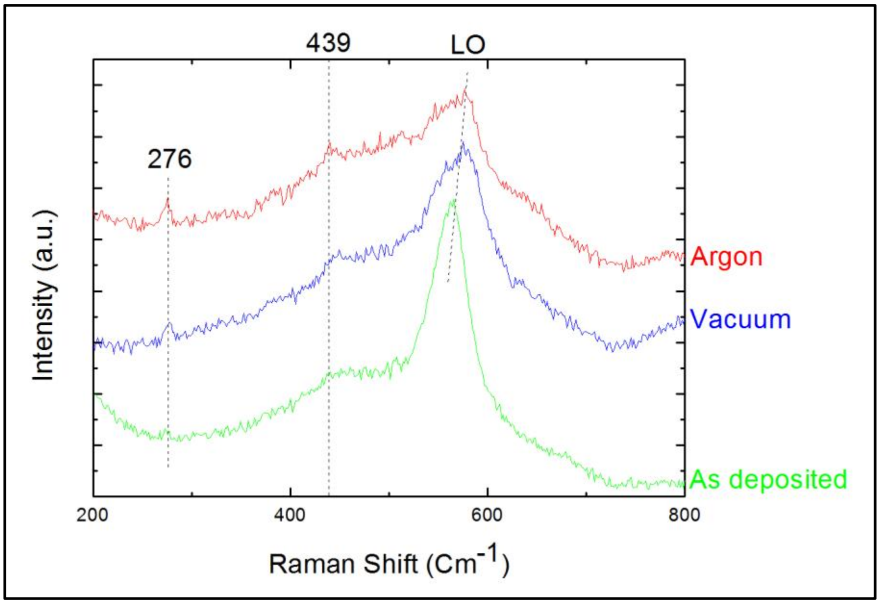

Figure 4.35: Raman spectra with 457nm excitation of samples deposited in 2Pa of oxygen and annealed in vacuum and argon at 500°C.

In figures 4.34 and 4.35, Raman spectra of samples annealed in argon and vacuum were compared with samples as deposited. It is possible to see the LO shift to higher wavenumber after annealing in both case, this shift is more in case of argon compare with vacuum. And also E_2^{high} peak is more intense in case of annealing in argon atmosphere. In samples annealed in argon atmosphere, argon atmosphere don't let oxygen atoms leave surface easily, but in case of annealing in vacuum they can leave surface more easily. This matter can describe the lower intensity of E_2^{high} in case of vacuum compare with argon atmosphere. In both case we have some effects such as recrystallization related to reduction of disorders and defects, it is possible to see the effect of this recrystallization in reduction of LO band. At the other hand oxygen atoms leave surface of the films, this matter caused the less intensity of the E_{2high} peak in case of vacuum compare with argon. In figure 4.33, we can see another peak around 276cm^{-1}; as we said before according to literature this peak is related to the aluminum doping and activation of B_2 silent mode. This peak is more intense in Raman spectra with 457nm excitation of samples after annealing.

4.7 Conclusion

In Raman spectra of AZO and ZnO sample deposited in pure oxygen, with increasing oxygen pressure the intensity of LO band decreased and intensity of E_2^{high} peak increased. This matter is related to the reduction of oxygen vacancy with increase of oxygen pressure; and also at lower oxygen pressure zinc excess cause resonance effects for LO modes in the visible range due to the presence of impurity states. At higher oxygen pressure, samples have open morphology and also oxygen stoichiometry caused insulating films.

With increasing deposition pressure, the morphology of samples was changed from compact to porous. At pressure lower than 10Pa, samples have columnar structures and at pressure higher than 100Pa, samples have tree-like nanostructure.

We can see a peak in Raman spectra with 457nm excitation at around 330cm^{-1} related to $E_2^{high} – E_2^{low}$ multi phonon process for ZnO samples deposited in 10Pa or higher pressure of oxygen. For AZO samples deposited in pure oxygen, it is possible to see this peak in 50Pa or higher pressure of oxygen.

Aluminum doping caused further disorder and more enhancement of LO mode. Presence of aluminum doping induced activity of B_2 modes and surface phonon modes at around $276cm^{-1}$ and $510cm^{-1}$ respectively.

There isn't any significant change in AZO compact samples after aging, but in porous samples we can see a reduction of LO band and increase of E_2^{high} mode related to recrystallization and reduction of defects and disorders.

We can deposit sampled with open morphology but low oxygen content with mixed atmosphere of oxygen and argon. In these samples the morphology is related to total pressure and oxygen vacancy and conductivity is related to oxygen partial pressure.

Annealing of samples caused the reduction of disorders and defects, this reduction caused the reduction of LO band, higher annealing temperature caused higher kinetic energy and more reduction of disorder and defects and as result more reduction of LO band. Annealing in vacuum leads oxygen atoms leave the surface and reduction of oxygen content at one hand and reduction of disorders and defects at the other hand; reduction of oxygen content decrease the intensity of E_2^{high} mode and reduction of disorders and defects increase the intensity of E_2^{high} mode. But annealing in argon atmosphere reduces the disorders and defects and also argon atmosphere don't let oxygen atoms to leave the film.

References

[1] E. Fortunato, D. Ginley, *et al.* ; Mrs Bulletin 32 (2007) pp. 242 – 247.

[2] P.P. Edwards, A. Porch, *et al.* ; Dalton Trans. (2004) pp. 2995 – 3002.

[3] K. Matsubara, P. Fons, *et al.* ; Thin Solid Films 422 (2002) pp. 176 – 179.

[4] S.S. Lo, D. Huang, *et al.* ; J. Phys. D: Appl. Phys. 42 (2009).

[5] M. Gratzel ; Nature 414 (2001) pp. 338 – 344.

[6] T. Minami, T. Miyata ; Thin Solid Films 517 (2008) pp. 1474 – 1477.

[7] B.Z. Dong, H. Hu, *et al.* ; Journal of Applied Physics 103 (2008).

[8] P.R. Willmott, J.R. Huber ; Reviews of Modern Physics 72 (2000) pp. 315 – 328.

[9] Z. Fan, J.G. Lu ; Journal of Nanoscience and Nanotechnology 5 (2005) pp. 1561 – 1573.

[10] L. Schmidt-Mende, J.L. MacManus-Driscoll ; Materialstoday 10 (2007) pp. 40 – 48.

[11] H. Bahadur, S.C. Garg, *et al.* ; “Characterization of ZnO Thin Films”.

[12] S.J. Pearton, D.P. Norton, *et al.* ; Materials Science 50 (2005) pp. 293 – 340.

[13] http://www.azom.com/article.aspx?ArticleID=4522

[14] K.J. Chen, T.H. Fang, *et al.* ; Applied Surface Science 254 (2008) pp. 5791 – 5795.

[15] J.T. Chen, J. Wang, *et al.* ; Applied Surface Science 255 (2009) pp. 3959 – 3964.

[16] D. Song ; Applied Surface Science 254 (2008) pp. 4171 – 4178.

[17] L.M. Li, Z.F. Du, *et al.* ; Sensors and Actuators B 147 (2010) pp. 165 – 169.

[18] N.D. Md Sin, M. Fuad Kamel, *et al.* ; Advances in Materials Science and Engineering (2011).

[19] S. Choopun, N. Hongsith, *et al.* ; J. Am. Ceram. Soc. 91 [1] (2008) pp. 174 – 177.

[20] Ü. Özgür, Y.I. Alivov, *et al.* ; Journal of Applied Physics 98 (2005).

[21] M. Suchea, S. Christoulakis, *et al.* ; Thin Solid Films 515 (2007) pp. 6562 – 6566.

[22] Z. Deng, C. Huang, *et al.* ; J. Mater Sci.: Mater Electron 21 (2010) pp. 1030 – 1035.

[23] G.J. Exarhos, S.K. Sharma ; Thin Solid Films 270 (1995) pp. 27 – 32.

[24] J. Hong, H. Paik, *et al.* ; Phys. Status Solidi A 206, No. 4 (2009) pp. 697 – 703.

[25] R.K. Shukla, A. Srivastava, *et al.* ; Journal of Crystal Growth 294 (2006) pp. 427 – 431.

[26] S. Venkatachalam, Y. Iida, *et al.* ; Superlattices and Microstructures 44 (2008) pp. 127 – 135.

[27] K.C. Park, D.Y. Ma, *et al.* ; Thin Solid Films 305 (1997) pp. 201 – 209.

[28] P. Banerjee, W.J. Lee, *et al.* ; Journal of Applied Physics 108 (2010).

[29] B. Joseph, P.K. Manoj, *et al.* ; Ceramics International 32 (2006) pp. 487 – 493.

[30] Q. Zhang, C.S. Dandeneau, *et al.* ; Adv. Mater. 21 (2009) pp. 4087 – 4108.

[31] G.J. Exarhos, X.D. Zhou ; Thin Solid Films 515 (2007) pp. 7025 – 7052.

[32] F.K. Shan, Y.S. Yu ; Journal of the European Ceramic Society 24 (2004) pp. 1869 – 1872.

[33] R. Vinodkumar, I. Navas, *et al.* ; Applied Surface Science 257 (2010) pp. 708 – 716.

[34] S. Sultana ; “RF Magnetron Sputtering system”.

[35] P.J. Kelly, R.D. Arnell ; Vacuum 56 (2000) pp. 159 – 172.

[36] S. Swann ; Phys. Technol. 19 (1988) pp. 67 – 75.

[37] J.H. Park ; Journal of the Korean Physical Society 49 (2006) pp. S584 – S588.

[38] H.U. Krebs, M. Weisheit, *et al.* ; Advances in Solid State Physics 43 (2003) pp. 505 – 517.

[39] H.M. Christen, G. Eres ; J. Phys. : Condens. Matter 20 (2008).

[40] A.V. Singh, R.M. Mehra, *et al.* ; Journal of Applied Physics 90 (2001) pp. 5661 – 5665.

[41] J.H. Lee, C.Y. Chou, *et al.* ; Nanotechnology 20 (2009).

[42] R.C. Scott, K.D. Leedy, *et al.* ; Journal of Crystal Growth 324 (2011) pp. 110 – 114.

[43] L.C. Tien, S.J. Pearton, *et al.* ; J. Mater. Sci. 43 (2008) pp. 6925 – 6932.

[44] Z. Xin, W. Shi-Qi, *et al.* ; Chinese Phys. 15 (2006) pp. 199 – 202.

[45] H. Kim, J.S. Horwitz, *et al.* ; Thin Solid Films 420 – 421 (2002) pp. 107 – 111.

[46] J.M. Lackner ; Thin Solid Films 494 (2006) pp. 302 – 306.

[47] E.L. Papadopoulou, M. Varda, *et al.* ; Thin Solid Films 516 (2008) pp. 8141 – 8145.

[48] W.J. Lee, C.R. Cho, *et al.* ; Journal of the Korean Physical Society 47 (2005) pp. S296 – S299.

[49] G. Fang, D. Li, *et al.* ; Vacuum 68 (2003) pp. 363 – 372.

[50] C. Lennon, R.B. Tapia, *et al.* ; Journal of Electronic Materials 38 (2009) pp. 1568 – 1573.

[51] B.Y. Oh, M.C. Jeong, *et al.* ; Journal of Crystal Growth 281 (2005) pp. 475 – 480.

[52] W. Yang, Z. Wu, *et al.* ; Thin Solid Films 519 (2010) pp. 31–36.

[53] A.E. Jimenez-Gonzalez; Journal of Solid State Chemistry 128 (1997) pp. 176 – 180.

[54] R.W. Miles, G. Zoppi, *et al.* ; Materialstoday 10 (2007) pp. 20 – 27.

[55] A.C. Mayer, S.R. Scully, *et* al. ; Materialstoday 10 (2007) pp. 28 – 33.

[56] H.H Li, P.Y. Yang, *et al.* ; IEEE Electron Device Letters 32 (2011) pp. 928 – 930.

[57] S. Yun, S. Lim ; Journal of Solid State Chemistry 184 (2011) pp. 273 – 279.

[58] S. Yun, J. Lee ; Journal of Physics and Chemistry of Solids 71 (2010) pp. 1724 – 1731.

[59] D. J. Gardiner, “Practical Raman spectroscopy”, Springer-Verlag (1989).

[60] P. Bruesch, “Phonons: Theory and Expriments II”, Springer-Verlag (1986).

[61] T. C. Damen, S. P. S. Porto, *et al.* ; Physical review 142 (1966) pp. 570 – 574.

[62] J. M. Calleja, M. Cardona ; Physical review B 16 (1977) pp. 3753 – 3761.

[63] J. Serrano, A. H. Romero, *et al.* ; Physical Review B 69 (2004) 094306.

[64] M. S. Jang, M. K.Ryu, *et al.* ; Current Applied Physics 9 (2009) pp. 651 – 657.

[65] J. F. Scott ; Physical Review B 2 (1970) pp. 1209 – 1211.

[66] C. Bundesmann, N. Ashkenov, *et al.* ; Applied Physics Letters 83 (2003) pp. 1974 – 1976.

[67] M. Tzolov, N. Tzenov, *et al.* ; Thin Solid Films 379 (2000) pp. 28 – 36.